Combination of mmWave Imaging and Communications for Simultaneous Localization and Mapping

by

Mohammed A M S A Aladsani

A Thesis Presented in Partial Fulfillment
of the Requirements for the Degree
Master of Science

Approved June 2019 by the
Graduate Supervisory Committee:

Georgios Trichopoulos, Chair
Constantine Balanis
Ahmed Alkhateeb

ARIZONA STATE UNIVERSITY

August 2019

ABSTRACT

In this thesis, the synergy between millimeter-wave (mmWave) imaging and wireless communications is used to achieve high accuracy user localization and mapping (SLAM) mobile users in an uncharted environment. Such capability is enabled by taking advantage of the high-resolution image of both line-of-sight (LoS) and non-line-of-sight (NLoS) objects that mmWave imaging provides, and by utilizing angle of arrival (AoA) and time of arrival (ToA) estimators from communications. The motivations of this work are as follows: first, enable accurate SLAM from a single viewpoint i.e., using only one antenna array at the base station without any prior knowledge of the environment. The second motivation is the ability to localize in NLoS-only scenarios where the user signal may experience more than one reflection until it reaches the base station. As such, this proposed work will not make any assumptions on what region the user is and will use mmWave imaging techniques that will work for both near and far field region of the base station and account for the scattering properties of mmWave. Similarly, a near field signal model is developed to correctly estimate the AoA regardless of the user location.

This SLAM approach is enabled by reconstructing the mmWave image of the environment as seen by the base station. Then, an uplink pilot signal from the user is used to estimate both AoA and ToA of the dominant channel paths. Finally, AoA/ToA information is projected into the mmWave image to fully localize the user. Simulations using full-wave electromagnetic solvers are carried out to emulate an environment both in the near and far field. Then, to validate, an experiment carried in laboratory by creating a simple two-dimensional scenario in the 220-300 GHz range using a synthesized 13-cm linear antenna array formed by using vector network analyzer extenders and a one-

dimensional linear motorized stage that replicates the base station. After taking measurements, this method successfully reconstructs the image of the environment and localize the user position with centimeter accuracy.

ACKNOWLEDGEMENTS

I thank God first and foremost for everything that he blessed me with. Then, a special thanks to my mentor and advisor Prof. George Trichopoulos for his support, guidance, and advice that helped me achieve this level and earn my master's degree and aim further toward my doctorate. My thanks also to the committee members Prof. Ahmed Alkhateeb, and Prof. Constantine Balanis for their contribution to my studies and my thesis defense. I would like to thank also Yiran Cui for all his help for computer simulations to support this thesis and all other lab members for their advice and support

I would like to also express my utmost appreciation and love to my family. My father and mother for their unyielding love and patient while I'm away pursuing my studies abroad. My sisters, who are just there any time to listen and support me and ease any hardships I encountered. My thanks are also extended to all my friends I met here in Arizona who let me feel I'm not that far from home.

I could not start my journey without my scholarship from Kuwait University, I thank them for their faith and trust in selecting me to peruse my grad studies abroad.

TABLE OF CONTENTS

Page

LIST OF FIGURES

Figure Page

Figure Page

Figure Page

Figure Page

Figure Page

CHAPTER 1

INTRODUCTION

Since the beginning of history, mankind desired to know their location and familiarize with the lay of the land to be able to travel around and trade with others. Seamen used the stars to estimate their position in the ocean and direct their ships to a destination while traveling merchants used known landmarks to guide their caravans around in the land. With the advent of electricity, people sought other methods to position themselves or objects of interest that do not rely on optical vision and provide more accurate information. One of the early methods was the invention of the radar in the early 20th century where it was first used to detect ships and avoid crashing with each other in foggy weather[1]. Fast forward to today, almost every aspect of daily life is using some form of positioning, mapping or both, from car navigation to autonomous cleaning robots in apartments. Thus, the concept of simultaneous localization and mapping (SLAM) was born.

Simultaneous localization and mapping is defined as the ability of a robot or a system to identify its environment, create a three-dimensional map, and acquire its current position[2]. One of the important factors that quantify the effectiveness of SLAM is the ability to localize and map the object of interest with high accuracy. Since millimeter waves (mmWaves, 30-300 GHz) have short wavelengths, high spatial resolution imaging can be achieved [3], [4] which, as we propose in this thesis, it can be exploited for high accuracy SLAM. As such ,SLAM can be implemented in various applications, including self-driving vehicles where nearby vehicles or crossing

pedestrians are identified to avoid accidents, assisted living tools by which vital signs and monitored and correlated with the current position to determine whether an injury occurred or not, and virtual/augmented reality devices where precise knowledge of the location of the surrounding objects provides the desired realism in the user's perceived environment [5]–[9].

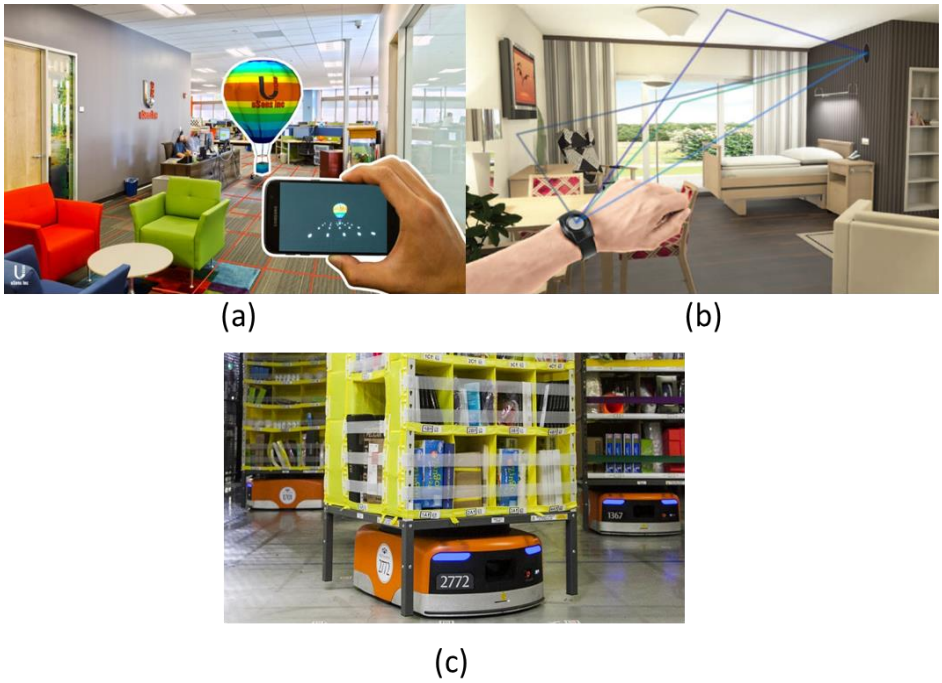

Figure 1.1- SLAM applications. A) Augmented reality enhancement [8]. B) Assisted living devices support [5]. C) autonomous robot navigation [9].

One of the fundamental approaches for localization is the time-of-arrival (ToA) or also known as time-of-flight (ToF). ToA can be defined as the time that took a signal generated by a source to travel and reach a receiver. The receiver can estimate the location of the source by multiplying the time with the speed of the signal in the medium, usually, the medium is considered as free space. This type of information is commonly

used in communications systems where the location of a mobile station (a user or device) is needed to better enhance the performance of such system such as more throughput or provide an extra service that the mobile station can use this information for. A well-known example that uses ToA is global positioning system or commonly known as GPS where a group of 24 synchronized satellites that orbit the earth and broadcast their location to a mobile device on earth that records the ToA and estimate the distance from each satellite to determine its position[10]. The basic concept for localization using ToA. Consider a scenario where a source (mobile station) in free space is transmitting a signal at time t_1, then a receiver records this signal at time t_2 , it follows that the distance *R* between the source and the receiver can be calculated as [11]:

$$R = (t_2 - t_1) * c_0 \qquad (3-20)$$

If we consider all the possible points formed by that distance *R*, then they will lie on a circle of radius *R*. Hence, it can be inferred that for a two-dimensional scenario at least three known receivers are needed to localize the source by the intersection of their distance projection circles as shown in figure 1.2. This method is also known as "trilateration".

However, this localization approach requires a strict synchronization between the transmitter and the receiver as any deviation will results in inaccuracy in time and therefore an error in localization. This type of synchronization is achieved by using an accurate time instrument which will add complexity and cost to the system [12]. Additionally, this method assumes a line-of-sight between the source and all receivers, as any multipath from the source to one receiver would translate to a different time delay, hence the distance *R* will be calculated erroneously. It is worth mentioning, that by adding the angle of arrival (AoA) information that is estimated from the induced phase shift on the multiple antennas of the access point (AP) will simplify the problem for localization in ToA. As this will result in reducing the requirement in principle to only one receiver compared to three when there is no AoA information as shown in figure 1.2.

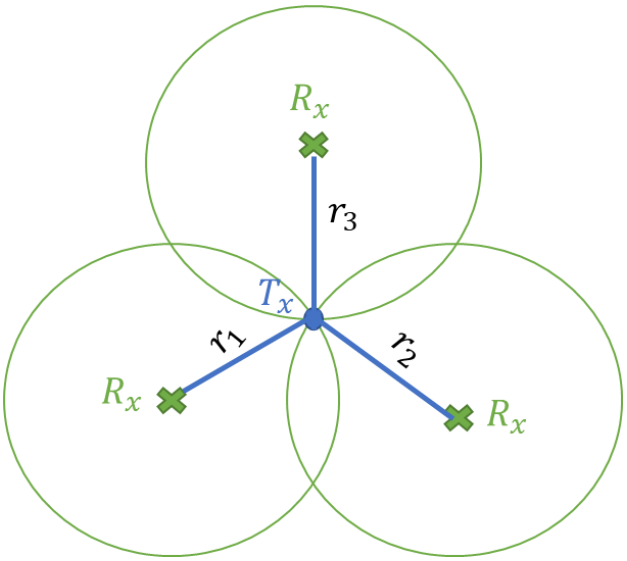

Figure 1.2-Source localization using ToA from 3 known receivers. By intersecting their distance projection circle the location of the source is estimated

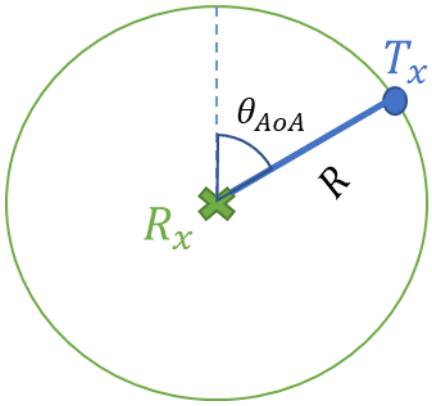

Figure 1.3-Source localization by combining AoA and ToA.

By relaxing the strict synchronization between the source and the receivers time difference of arrival (TDoA) is used for localization. As there is no need in TDoA for the transmitter to be in sync with the receivers, but the receivers themselves are required to be in sync with each other. Hence, the source position can be determined by measuring the difference in time of the signal received between the two receivers *i* an *j*, and when multiplied by the speed of the signal this will result in the difference of range as:

$$R_{i,j} = c_0 * \Delta t_{i,j} \qquad (3-21)$$

The possible set of points for any two receivers *i* and *j* with range difference $R_{i,j}$ due to a source will lie on a hyperboloid as show in figure 1.4 The equation in 2D is given by [11]:

$$R_{i,j} = \sqrt{(x_i - x)^2 + (y_i - y)^2} - \sqrt{(x_j - x)^2 + (y_j - y)^2} \qquad (3-22)$$

Where $(x_i, y_i), (x_j, y_j)$ are the known coordinates for receiver *i,j* , and (x, y) are the coordinates of the source that is to be located. Similar to ToA, at least 3 receivers are needed to localize the user as this will generate 3 hyperboloids that can be intersected and

solve for the user location. To solve this problem a nonlinear regression or try to linearize the problem by using Taylor series expansion and then solve it numerically [11].

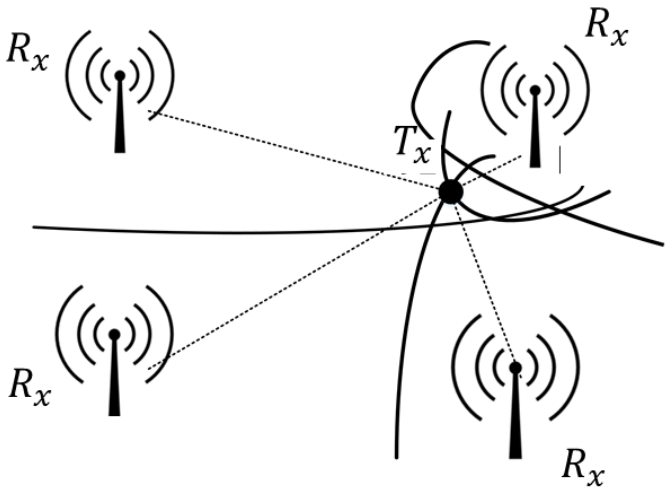

Figure 1.4- Source localization using TDoA approach. For each two receivers a hyperboloid is calculated, then by the intersection of these hyperboloids, the user location is estimated [11].

One of the early work in SLAM is exploiting the received signal strength known as received signal strength indicator (RSSI) of Wi-Fi signals in wireless sensors environment for localization [13]. By relating the RSSI to the signal attenuation model due to path loss, the traveled distance can be estimated. This approach suffers an average error of 1 meter in localization which can be considered high for small indoor scenario. The reason for this error is that reflections/diffraction from metal objects inside the room are not considered and this impacts the measured RSSI resulting in distance estimation error. Z. Wei et al. extended RSSI localization in mmWaves systems by adding AoA [14]. This was achieved by creating a database "fingerprint" of all RSSI/AoA's of

possible candidate locations defined here as a reference point, then match the recorded RSSI and AoA of a source with this fingerprint database to estimate the source position as shown in figure 1.5. While this approach exploited the narrow beamwidth that mmWaves provide to reduce estimated error in a very large indoor environment, it suffered from computational complexity due to the need for a big number of APs or/and adding more reference points into the database to achieve high accuracy. WiFi in conjunction with OFDM -based user localization scheme that uses communication channel estimation and RSSI to resolve for AoA/range that leads to the user location by using off-the-shelf WiFi APs was developed in [15]. A fine estimation of AoA is achieved by exploiting the fact that the induced phase shift is the same across all the OFDM subcarriers for the given bandwidth of 40 MHz hence, the number of antennas in the APs can be artificially increased in post-processing by number of physical antennas times the number of subcarriers which will lead to a finer estimation on AoA. Although this scheme achieves sub-meter accuracy, it heavily relies on the number of available APs and the performance is degraded when there is two or less AP in LoS.

In [16], user is localized by using a single WiFi AP that uses (ToA) information only by exploiting the fact that the accumulated phase delay recorded at the AP is directly related to ToA. By transmitting pilot signals from the user to the AP over different WiFi frequency bands results in different measured phase delays. Then, these phase delays are combined and processed to acquire the location of the user as the distance is ToA multiplied by the speed of propagation. While this method achieves an average localization accuracy of 0.65 m, it is not scalable because it has been developed with a single AP in mind and neglect the impact of other APs on the localization. Also, the

hoping between different WiFi bands can negatively impact the performance of communications between the other users and the AP as the localization process will use resources all over the bands that can be utilized for communication links.

Others used frequencies below 6 GHz to support mmWave systems for localization due to well established and robust sub 6GHz AoA estimation techniques as seen in figure 1.6 [17]. AoA is estimated with respect of sub 6GHz band and is fed to the mmWave system to reduce beam training overhead; then it is paired with mmWave ranging to provide an estimate of the user location. The drawback is the requirement of having both sub 6 GHz and mmWave hardware presented at both the user and the base station. Also, not taking into account the difference in material interaction between sub 6GHz and mmWave for AoA estimation will result in an inaccurate estimate as the multipath effect and the reflection/scattering of mmWave are not considered.

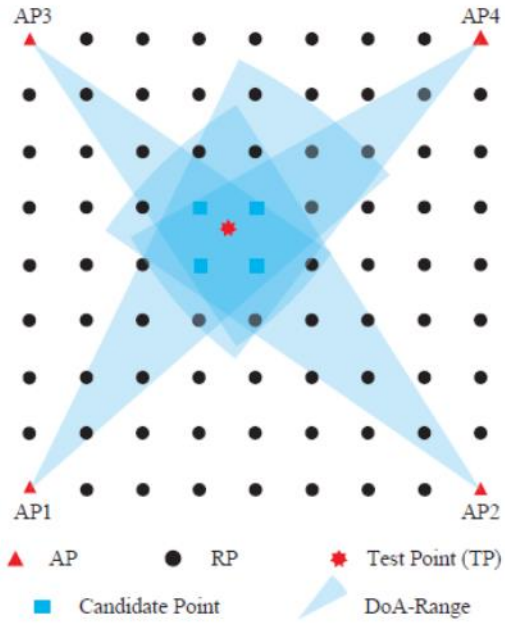

Figure 1.5-Joint RSSI and AoA localization. A database containing all possible RSSI/AoA for every reference point in the environment is created, then the user is compared from his RSSI/AoA against this database to estimate his position [14].

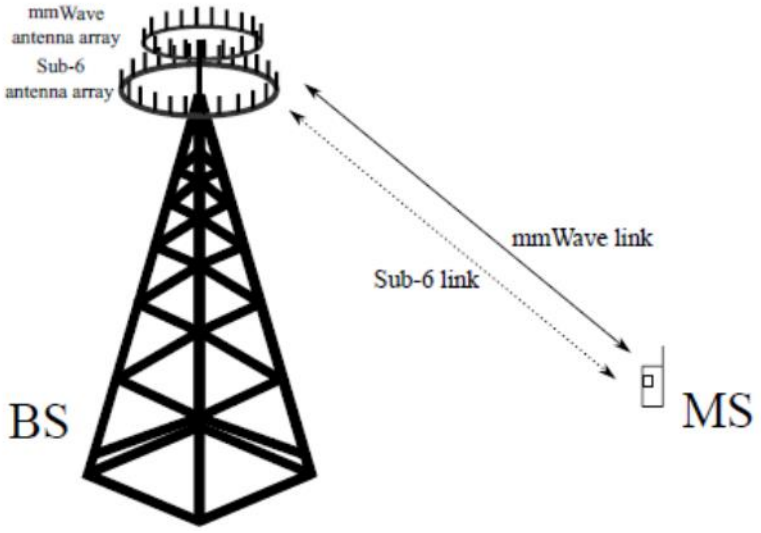

Figure 1.6– Exploiting pre-existing sub 6 GHz resources to support mmWave localization estimation. Well known sub 6 GHz estimation tools are used to acquire information and feed it to mmWave system to improve the estimation process [15].

In [18], the difference between AoAs of several APs or angle difference of arrival (ADoA) were used to estimate localize the user. First, the locations of APs are estimated by recording the AoA from three different AP's with respect of the user and subtracting them. Then the intersection of the arcs that are the loci of all possible points that satisfies this angle difference is the location estimate of the APs as shown in figure 1.7. Finally, by estimating the location of all APs, the user is localized in the same manner with the knowledge of APs positions. They are able to localize the user in line-of-sight (LoS) and line-of-sight with non-line-of-sight (NLoS) scenarios within sub-meter accuracy and provide a partial mapping of the environment without prior knowledge. However, the approach requires a total of at least 4 APs and one of them must be in LoS to properly work.

An algorithm that exploits the combined information from AoA, angle of departure (AoD) and ToA is used to estimate the position and the orientation of the user [19]. This algorithm reaches the Cramér–Rao lower bound (CRLB) for a single mmWave transmitter in the presence of scatterers which defines the best user position and the orientation estimation achievable. However, it cannot localize the user when there is more than one bounce in the NLoS or the AP is in a scenario where there is only NLoS with no LoS path present. As a general remark, current SLAM methods are limited by the inability to 1) localize in NLoS path only, 2) produce a full high-resolution map of the environment. Therefore, the objective of this thesis is to develop a SLAM algorithm that uses mmWaves to provide a map of the environment and localize a user with high accuracy even in a scenario where there is only NLoS path and with no a priori knowledge of the environment.

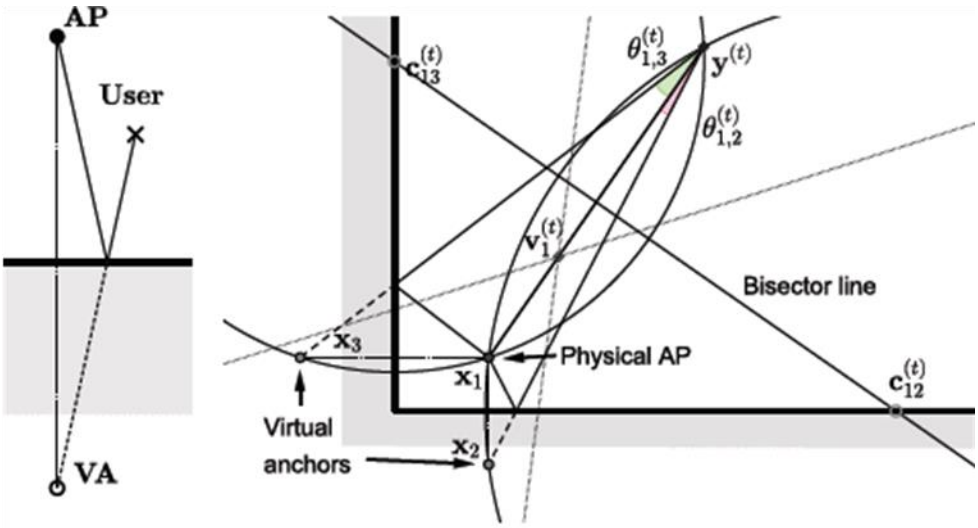

Figure 1.7- Localization using the difference of the estimated AoAs of several access points. This difference is used first to estimate the location of APs and then localize the user [16].

1.1 Outline of the Thesis

The organization of this thesis as follows: in chapter 2 the theory of mmWave imaging and around the corner imaging are discussed. Then in chapter 3, received signal model will be analyzed both in the near and far field and provide the array factor/steering vector associated with that model, and in the same chapter, this thesis approach for SLAM will be developed by combining both mmWave imaging and AoA/ToA information. After that in chapter 4, simulations and measurements of the proposed approach will be presented. Finally, chapter 5 will be the conclusions and the future work of this thesis.

CHAPTER 2

BASIC CONCEPTS OF ACTIVE MILLIMETER-WAVE IMAGING

In this chapter, the theory of active millimeter-wave imaging will be discussed. Then, NLoS imaging will be presented with measurements result to demonstrate the capability of using mmWave imaging system for NLoS objects scenarios.

2.1 Active Millimeter-Waves Imaging Systems

Active imaging systems illuminate the scene and then receives the signals scattered in the surrounding environment. One of the applications of active mmWave imaging is concealed weapon detection, as mmWaves can penetrate fabric and hidden weapons will present a strong reflection in the mmWaves image that can be detected and identified. [4], [20]. A big concern for mmWaves imaging is as the distance increases the cross-range resolution decreases which needs an increased aperture size and thus the weight for the imaging system. In [20] they preserve the resolution as the distance increases by employing lens that collimates the beam. However, this comes at the cost of big lens and heavy equipment that makes scalability hard as shown in figure 2.1.

As such, lensless imaging systems can be more practical if realized in large apertures due to the low profile and small weight[4], [21], [22]. Active mmWave systems can employ different reconstruction approaches that can be used on 2D planar based systems and able to reconstruct 3D images from the collected measurements from the 2D surface such as backward propagation and beam steering and can be further enhanced by employing digital signal processing techniques such as fast Fourier transforms and multiple signal Classification (MUSIC)[4], [23] . Thus, they are lensless and can have a compact form factor compared to lens-based systems while having a high spatial

resolution. In this chapter, the focus of our discussion is on planar systems due to its low weight and scalability that can be used in conjunction with communication systems.

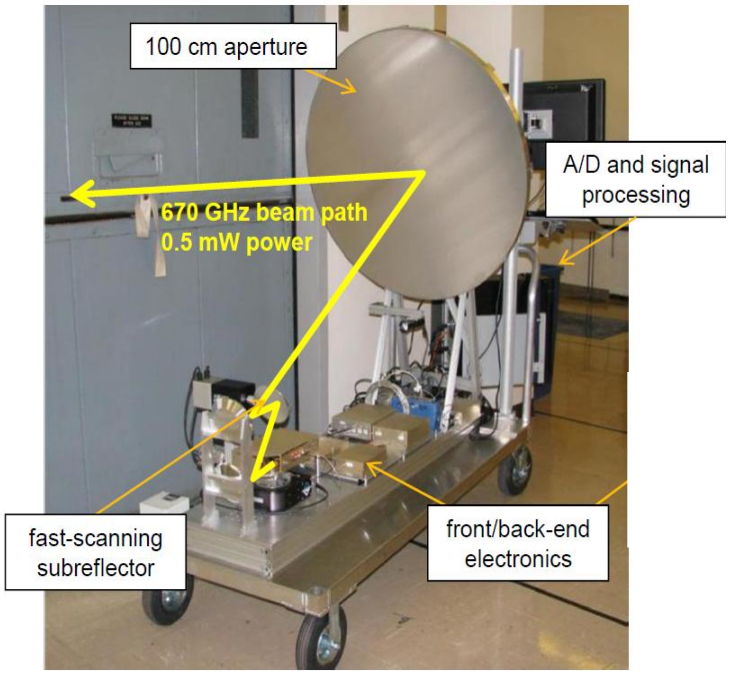

Figure 2.1- Proposed active imaging system in [17] highlighting the heavy equipment and lens.

2.2 Backward Propagation using Fourier Transform Method for Imaging

There are many techniques in literature and practice for getting an image of an object, one such technique is called the Backward Wave Imaging. If that object is illuminated by EM waves then the amplitude and phase of the reflected wave can be recorded by a receiving aperture, in which by applying the backward wave propagation algorithm, the object shape image can be reconstructed. The backward wave propagation method is implemented in this chapter by using FFT algorithm as described mainly in[4].

In this work, we focus on monostatic imaging systems where both the transmitter and the receiver lay on the same location. Nevertheless, this work can be generalized to multistatic imaging systems and SLAM performance is expected to be superior. The target domain is divided into n planes with distance z_n from transceiver plane, each is assumed to be flat and parallel to the imaging aperture as shown in Figure 2.1. Then, the transceiver/target planes are assumed to be coinciding with each other i.e. they share the same dimensions, and the x-y plane will be called cross-range axis and the distance from the transceiver plane to the target plane along the z-axis is called range axis. It is also assumed that the transceiver is located $(\bar{x}, \bar{y}, 0)$, and a point in the target plane z_n is at (x, y, z_n), and the transceiver illuminates the target over a band of frequencies.

The response of the system for a given wavenumber $k = \frac{\omega}{c_0}$ ($\omega = 2\pi f$, and c_0 is the speed of light in free space) and for a target that can be characterized by a reflectivity function $O(x, y, z) = \delta(x - x_t, y - y_t, z - z_n)$ [24], where x_t, y_t represents a point on the target plane is the sum of all points on the target planes multiplied by the phase travelled to theses points and given by:

$$s(\bar{x}, \bar{y}, k) = \iiint o(x, y, z) \times e^{-j2kr} dxdydz \qquad (2-1)$$

Where

$$r = \sqrt{(\bar{x} - x)^2 + (\bar{y} - y)^2 + (\bar{z} - z_n)^2} \qquad (2-2)$$

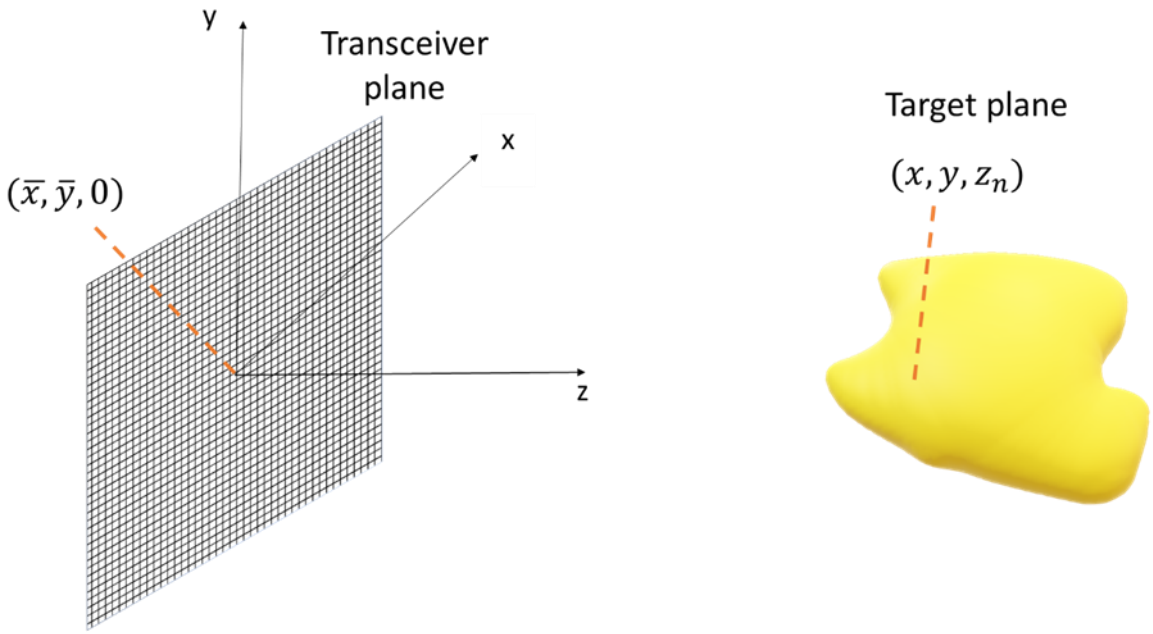

Figure 2.2 - Topology of an active monostatic mmWave imaging system. Transceiver/target plane is primed/unprimed coordinate respectively.

The phase term e^{-j2kr} in equation (2-1) models a spherical wave originating from the transceiver point $(\bar{x}, \bar{y}, 0)$. Using the method of stationary phase [25], [26] the spherical wave can be broken into an infinite sum of plane waves

$$e^{-j2kr} = e^{-j2k\sqrt{(\bar{x}-x)^2+(\bar{y}-y)^2+(\bar{z}-z_n)^2}} = \iint e^{-jk_x(\bar{x}-x)-jk_y(\bar{y}-y)-jk_z(\bar{z}-z_n)} dk_x dk_y \quad (2-3)$$

Where k_x, k_y, k_Z are the spatial frequencies of *x*, *y*, and *z* coordinate respectively.

Thus, by substituting equation (2-3) into (2-1) and dropping the distinction between primed and unprimed coordinate systems since both planes share the same coordinate system yields

$$s(x,y,k) = \iint \left[\iiint o(x,y,z) e^{-j(k_x x + k_y y + k_z z)}\, dxdydz \right] e^{jk_z z_n} e^{jk_x x} e^{jk_y y} dk_x dk_y \quad (2-4)$$

The term in the bracket represents the 3D spatial Fourier transform given by

$$O(k_x, k_y, k_z) = FT_{3D}[o(x,y,z)] = \iiint o(x,y,z) e^{-j(k_x x)} e^{-j(k_y y)} e^{-j(k_z z)}\, dxdydz \quad (2-5)$$

Then, equation (2-4) becomes

$$s(x,y,k) = \iint \left[O(k_x, k_y, k_z) \right] e^{jk_z z_n} e^{jk_x x} e^{jk_y y} dk_x dk_y \quad (2-6)$$

By using mathematical manipulations and Fourier pairs relations

$$s(x,y,k) = FT_{2D}^{-1}\{ [\, O(k_x, k_y, k_z)] e^{jk_z z_n} \} \quad (2-7)$$

$$S(k_x, k_y, k) = FT_{2D}[s(x,y,k)] = O(k_x, k_y, k_z) e^{jk_z z_n} \quad (2-8)$$

$$S(k_x, k_y, k) e^{-jk_z z_n} = O(k_x, k_y, k_z) \quad (2-9)$$

$$o(x,y,z) = FT_{3D}^{-1}\left[S(k_x, k_y, k) e^{-jk_z z_n} \right] \quad (2-10)$$

From the electromagnetic dispersion of plane waves

$$(2k)^2 = k_x^2 + k_y^2 + k_z^2 \quad (2-11)$$

$$k_z = \sqrt{4k^2 - k_x^2 - k_y^2} \quad (2-12)$$

Finally, the relationship between the received backscattered signals $s(x,y,k)$ and the scene's reflectivity function $o(x,y,z)$ (reconstructed image) is obtained from

$$o(x,y,z) = FT_{3D}^{-1}\left[FT_{2D}[s(x,y,k)] e^{-j\sqrt{4k^2 - k_x^2 - k_y^2} z_n} \right] \quad (2-13)$$

It is meaningful to give an expression for 2D imaging reconstruction as it will be used on later chapters, by following similar steps of equation (2-1) to (2-12) for a transceiver that illuminates targets at single cross range with a band of frequencies, the reconstructed 2D image is

$$o(y,z) = FT_{2D}^{-1}\left[FT_{1D}[s(y,k)]e^{-j\sqrt{4k^2-k_y^2}z_n}\right] \qquad (2-14)$$

2.3 Spatial Resolution and Sampling Criteria for the Monostatic Imaging System

An image can be represented in the spatial frequency domain by taking the Fourier transform across the spatial domain, this spatial frequency domain is commonly called k-space [27]. It is a function of the imaging aperture, antenna beamwidth, and the temporal bandwidth. This representation contains important details about the image and the system that generate this image. Such examples of those details are the resolutions of the image in both the cross range and range. An example of such space is shown in figure 2.2 [4].

2.3.1 Spatial Resolution of the Imaging System

The spatial resolution of an imaging system is important as it defines the fidelity of the image produced, and the amount of the details such an image contains. Spatial resolution depends on the information that is obtained from the spatial frequency domain of the system. For 3D spatial dimensions, the maximum spatial resolution at each axis in a Cartesian system is given by the relations of Fourier transform of equation (2-13) [28] :

$$\delta_x \approx \frac{2\pi}{\Delta k_x} \qquad (2-15)$$

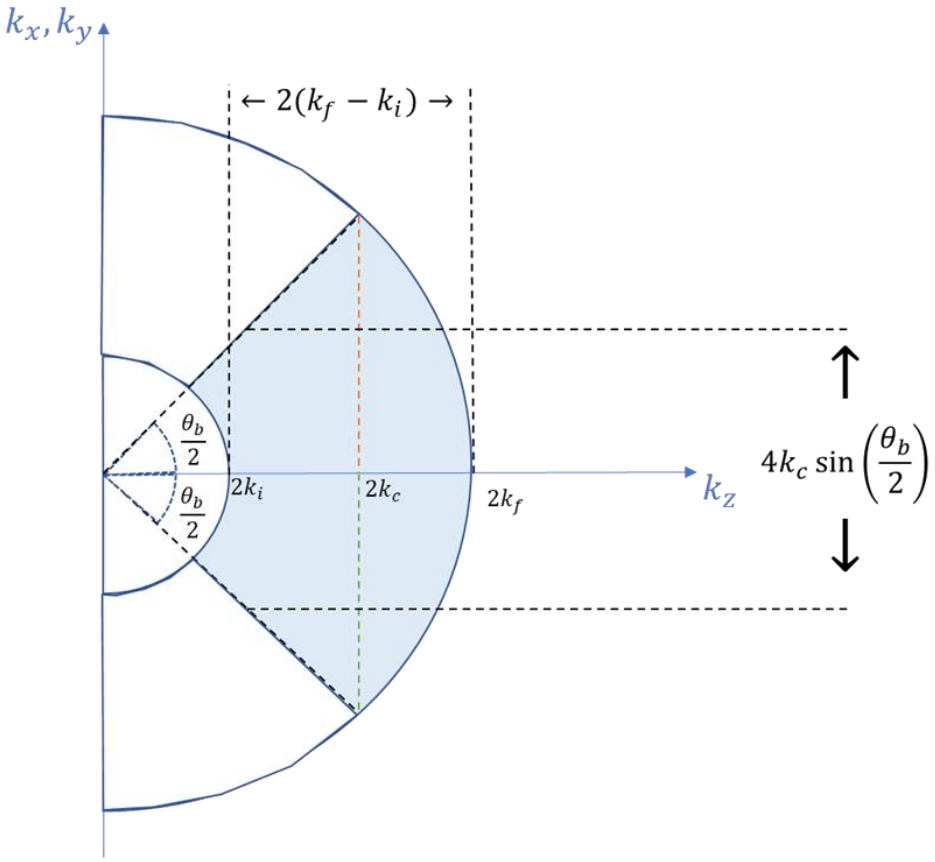

Figure 2.3- K space representation of a 3D imaging system operating at range of wavenumbers from $[k_i, k_f]$ with central wavenumber of k_c. The shaded area represents the spatial frequencies supported by a given imaging system [4].

$$\delta_y \approx \frac{2\pi}{\Delta k_y} \qquad (2-16)$$

$$\delta_z \approx \frac{2\pi}{\Delta k_z} \qquad (2-17)$$

By looking into figure 2.2 and assuming a square, then $\Delta k_{x,y}$ can be approximated by the width of a rectangle whose length in the cross range is given by [4]:

$$4k_c \sin\left(\frac{\theta_b}{2}\right) \qquad (2-18)$$

Where $k_c = \frac{2\pi}{\lambda_c}$ is the central wavenumber, θ_b is the lesser between the beamwidth of the antenna element or the angle subtended by the aperture. Similarly, the cross range resolution is given by [4]:

$$\delta_x = \delta_y \approx \frac{2\pi}{4k_c \sin\left(\frac{\theta_b}{2}\right)} = \frac{\lambda_c}{4 \sin\left(\frac{\theta_b}{2}\right)} \qquad (2-19)$$

Also, for an imaging system whose aperture *D* is smaller than the distance *R* of the object from the aperture, the cross range resolution can be simplified as [4]:

$$\delta_x = \delta_y \approx \frac{\lambda_c R}{2D} \qquad (2-20)$$

As for the resolution in range or the z-axis, the width is$\Delta k_z = 2(k_f - k_i)$ where k_f , k_i are the highest and lowest wavenumbers respectively. Therefore, the range resolution is approximated as [4]:

$$\delta_z \approx \frac{2\pi}{2(k_f - k_i)} = \frac{\pi}{\frac{2\pi}{c}(f_f - f_i)} = \frac{c_0}{2B} \qquad (2-21)$$

Where *B* is the bandwidth of the system. It is worth mentioning that equation (2-21) also represent the range resolution of a monostatic radar which is expected as this imaging system operates similarly to monostatic radars in principle.

2.3.2 Sampling Criteria

Since scattered data collection is based on synthetic aperture radar (SAR) which is discretized in nature. Then, the need to choose proper sampling for both SAR movement (cross-range axis samples), and the temporal frequency step size is important to ensure correct image formulation without any artifact or corruption. The sampling along SAR is impacted by several variables such as the selection of wavelength, distance from the target and its size, and how long is the SAR aperture. In general, proper sampling is ensured if the Nyquist criteria are met, which states the phase shift in the spatial frequency domain from one SAR sample point to the next does not exceed π rad. Therefore, for a sample spatial size of Δx, the phase shift should not exceed $2k\Delta x$ for the worst case i.e. the target is near or at the edge of aperture[4]. Hence,

$$2k\Delta x = \frac{4\pi}{\lambda}\Delta x < \pi \qquad (2-22)$$

$$\Delta x < \frac{\lambda}{4} \qquad (2-23)$$

Equation (2-23) represents the smallest sampling distance, however, achieving $\frac{\lambda}{4}$ is not practical for all cases as it requires more time to scan along the cross range. Depending on how far SAR is from the target and that the antenna beamwidth is usually less than 180^o , $\frac{\lambda}{4}$ is not necessary and practical system can choose a sample size in the order of $\frac{\lambda}{2}$ [4]. Similarly, the temporal frequency sampling need for focusing targets at a maximum range of R_{max} is selected such that the phase shift from one wavenumber to the next " Δk" does not exceed π , where the worst case is $2\Delta k R_{max} < \pi$, Therefore [4]

$$2\Delta k R_{max} = \frac{4\pi}{\Delta\lambda} R_{\max} \ < \pi \qquad (2-24)$$

$$\Delta f < \frac{c_0}{4R_{max}} \qquad (2-25)$$

Where Δf is the required temporal sampling frequency. From equation (2-25), the number of samples point $N_f = \frac{B}{\Delta f}$ can be related as :

$$\frac{\mathrm{B}}{N_f} < \frac{c_0}{4R_{max}} \qquad (2-26)$$

$$N_f > \frac{4R_{max}}{\frac{c_0}{B}} = \frac{2R_{max}}{\frac{c_0}{2B}} \qquad (2-27)$$

Or

$$N_f > \frac{2R_{max}}{\delta_z} \qquad (2-28)$$

It can be inferred from equation (2-27) that the selection of the number of frequency samples over a given bandwidth impacts the allowable maximum range to be imaged. This combined with equation (2-23) and (2-21) gives a general guideline for the selection of the design parameter of the imaging problem.

To summarize as a rule of thumb:

- Temporal bandwidth impacts range resolution, the higher the bandwidth the finer the range resolution is.
- Frequency step size or number of frequency points over a given bandwidth impact maximum unambiguous range, more frequency points lead to longer range.

- Sampling distance along SAR is best at $\frac{\lambda}{4}$, but if the target is moderately far from SAR and the beamwidth is narrow, $\frac{\lambda}{2}$ sampling can be sufficient for reliable and image reconstruction.

2.4 Non-Line of Sight Imaging Using Millimeter-Waves

MmWaves sit between microwaves and infrared (IR)/visible light with respect of the RF spectrum in an area that has been dubbed "THz gap" [22] as shown in figure 2.3. , and they are promising candidates for non-line-of-sight (NLoS) imaging since it exhibits traits of both microwaves and IR/visible light featuring both specular and diffuse reflection/scattering phenomena when bouncing off common building materials including wood, drywall, etc. Such materials exhibit a moderately rough surface with respect to mmWave wavelengths. As such, they can be modeled as lossy mirrors where a significant ratio of the incident energy is reflected specularly and the remaining power is diffused almost isotropically as illustrated in figure 2.4. [29], [30]

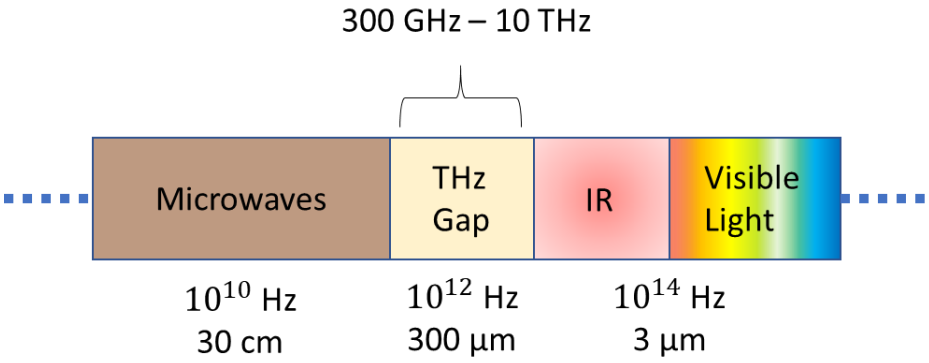

Figure 2.4- Portion of the EM spectrum highlighting the THz gap.

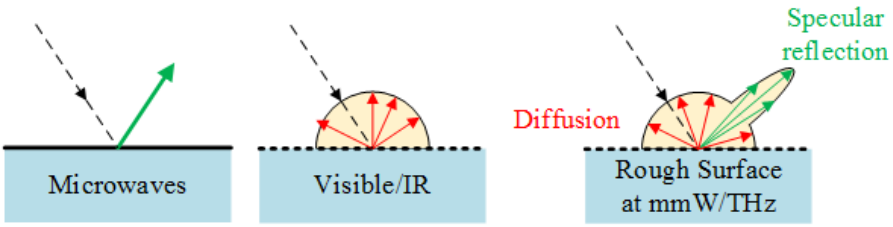

Figure 2.5- EM waves scattering with respect of wavelength compared to the surface. Microwaves reflect specularly as it sees the surface to be smooth, Visible/IR diffuses due the apparent roughness of the surface, mmWaves have both traits as it sees the surface as moderately rough.

What makes mmWave wave also interesting for imaging is that its short wavelengths allow high spatial resolution which contributes to the fidelity of the overall image. As a consequent of being an EM wave, it is not impacted by lower visibility including night, dust, smoke, and fog. By exploiting both high spatial resolution and scattering properties that mmWave waves provides, an NLoS imaging application where common building materials such as open wooden door of an office is used to "look around" and acquire a detailed image of what's inside the room as if the door is a mirror [31].

In this model as shown in figure 2.5, SAR is used to image an object and the reflecting surface by leveraging mmWave waves multipath propagation. It is first assumed that object is hidden from SAR by non-transparent occlusion with respect to mmWave i.e. no direct line-of-sight (LoS) path, the same non-transparent property is assumed on the object as well. Secondly, the reflecting surface (mirror) has a roughness that enables the mmWave wave to scatter both in the specular and the diffusion directions. Also, no prior information is known about the complete scene for both the

mirror and the object. Finally, although this method and SAR imaging techniques allow for 3D image reconstruction, for simplicity and experimental condition constrains 2D imaging (one cross range and range) is considered [31].

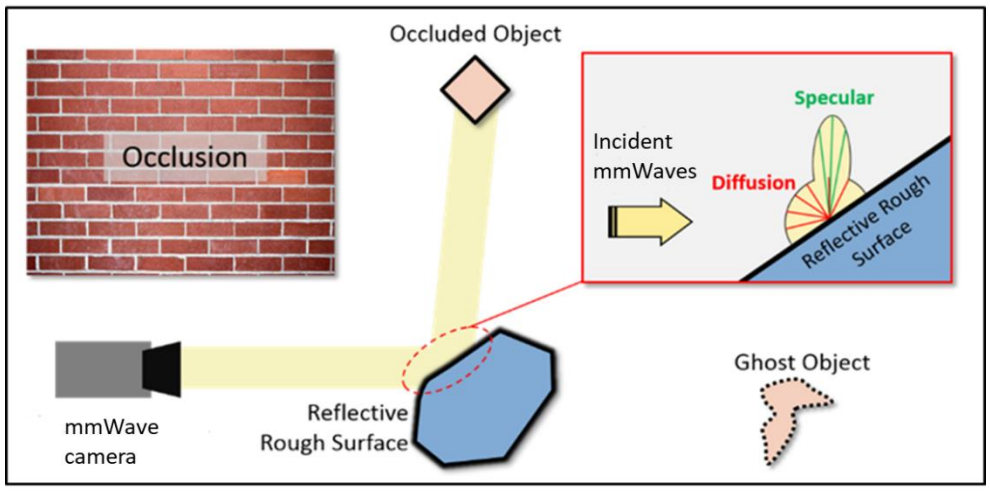

Figure 2.6-Representation of non-line-of-sight (NLoS) imaging. MmWaves generated from SAR are specularly and diffusely scattered from common material "reflecting surface" then exploited to image the NLoS object, occlusion is there to ensure that only NLoS path is present [31]. the hidden object appears as a ghost behind the reflective surface due to not accounting for the mmWaves multipath propagation.

This is done by using SAR that illuminates the scene by mmWave waves and record the scattered field data. Then the recorded data can be formatted and reconstrued as an image by using equation (2-14). It follows that by applying equation (2-14) into NLOS scenario similar to the one depicted in figure 2.5 without taking into account the multipath propagation and not identifying the reflecting surface by exploiting diffusion will lead into a raw image that does not represent the reality and needs to be corrected as shown in figure 2.5.

2.4.1 Identifying the Reflective Surface from Diffuse Scattering

As stated before, in the mmWave wave spectrum most common building material experience both a strong specular reflection and a significant diffuse scattering that can be measured. To demonstrate that, bistatic radar cross section (RCS) of metallic mirror vs calcium sulfate dihydrate (gypsum) known generally as drywall that has been compressed between paper sheets have been measured in the frequency of 330 GHz as shown in figure 2.6. It is shown that due to the roughness of the drywall, the diffuse scattering is significant and can be observed to be around -30dB compared to the maximum in average, yet the specular reflection is still strong and able to acquire the image of the hidden object from it. From the definition of the model shown in figure 2.5, the scattered signals due to the diffusion of the reflective surface will arrive earlier in time to SAR compared to the scattered signals from the hidden object which is expected due to the travel path of both scattered signals. This can be exploited with the geometry of the reflective surface to devise an algorithm that will differentiate between the hidden object and the reflective surface and their respective location, and at the same time create an image that will represent the true scene.

2.4.2 Image Correction for Non-Line-of-Sight Imaging

From the previous discussion, the algorithm makes the following assumptions : no object in the scene is transparent with respect to the frequency range used, the first object that appears in the raw image with respect to range is assumed to be the reflective surface and what is after the object is what will be dubbed as “ghosts” [31]. Then, the algorithm works as the following: First, the scattered mmWave wave data that has been recorded by SAR is collected. Then, the raw image is reconstructed using equation (2-14) and identify

the reflective surface and then map the ghost object into its correct location. Finally, the raw image is updated with corrected positions. This mapping process is done by translating these ghost objects into their correct locations by rotating each point after the reflective surface by an angle of (180-2 θ_i) degree with respect to that reflective surface as shown in figure 2.7 , where the center of rotation is at the intersection of the reflective surface and the line that connects the ghost object with the SAR [31].

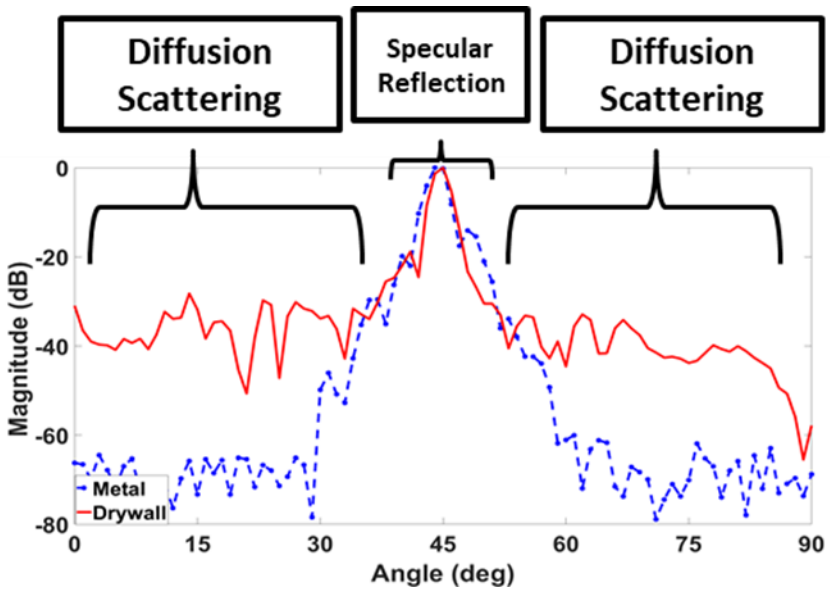

Figure 2.7- Bistatic RCS of metal mirror vs drywall @ 330 GHz, it is shown that mirror has stronger main lobe and lower sidelobes compared to drywall which is the expected case. Nevertheless, the drywall still exhibits strong main lobe and with an average of -30dB for the sidelobe which represents the diffusion scattering that still can be detected

2.4.3 Experimental Validation of Non-Line-of-Sight mmWave imaging

To test the capability of NLoS imaging system, an experiment replicating similar scenario like the model depicted in figure 2.5 is performed by using two vector network analyzer (VNA) extenders, two horn antennas, and a motorized linear translation stage that emulated a 12 cm monostatic SAR operating at a bandwidth of 100 GHz with frequency range between 220-320 GHz with 0.1 GHz sampling which yields about a

maximum range of 1.5 m with a resolution of 1.5 mm. Also, drywall was used as a reflective surface, and two metallic posts are placed in the scene as targets as shown in figure 2.9 [31].

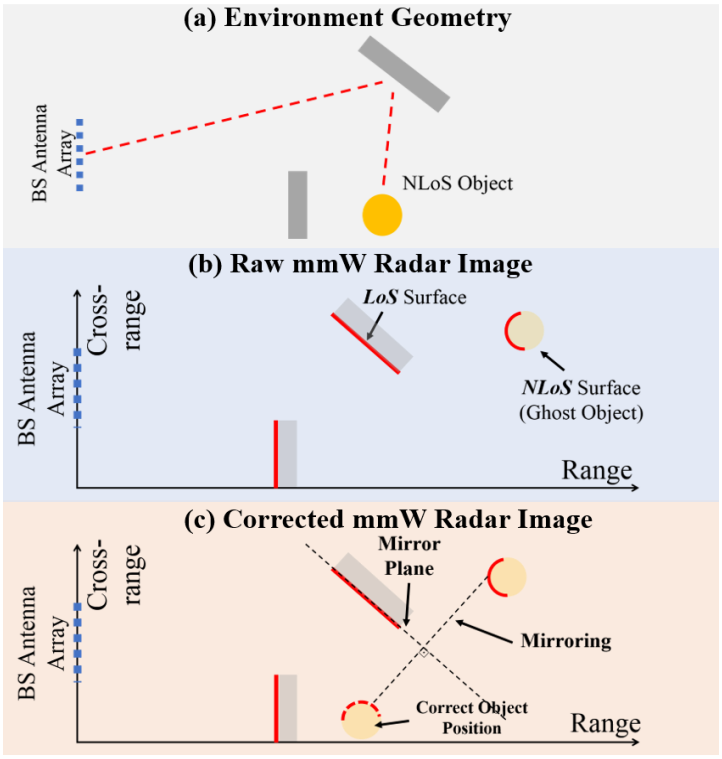

Figure 2.8-Image correction algorithm.a) The true geometery. b) the reconstructed Raw mmWave image. c) the corrected image, this is done by rotating each ghost object (180-$2\theta_i$) degree with respect of reflective surface into their respective correct position.

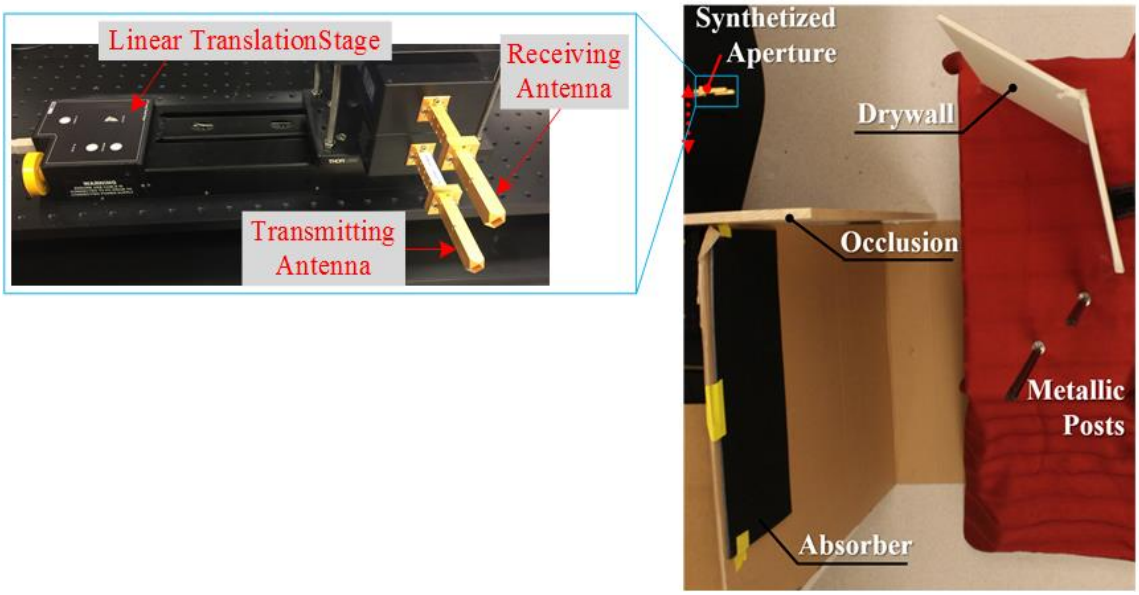

Figure 2.9- Experimental setup done in the lab; SAR is used to image the metallic post by exploiting mmWave wave interaction with drywall as a reflective surface. Occlusion is there to make sure only NLOS components are present, and absorber is used to avoid scattering from other objects in the lab. Inset: SAR is implemented by using a pair of transmitting/receiving antenna mounted over a linear translation stage [31].

The data collected is processed by a MATLAB script following equation (2-14) and reconstructs the raw image as shown, in figure 2.10 (a). In this raw image, the bright yellow lines represent the drywall surface due to diffusion scattering. The geometry of these points will be used as the mirror plane to correct the raw image following the discussion in section 2.3.2. The updated image is also shown in figure 2.10 (b). To further demonstrate the capability of this system, metallic posts were placed as targets and the algorithm was able to identify the posts and translate them to the correct position as shown in figure 2.11.

In this Chapter, the basic concepts of active mmWave imaging system were presented and analyzed and discussed the ability using mmWaves for high-resolution NLoS imaging by exploiting the diffuse scattering of mmWaves to image and identify the

reflective surfaces and image the NLoS object from the specular scattering. Then to illustrate the capability of using mmWaves for NLoS imaging, an experiment was carried out as mentioned in this chapter that was able to produce a 1.5 mm range resolution image, identify the reflective surface, and correct the image to reflect the true scene.

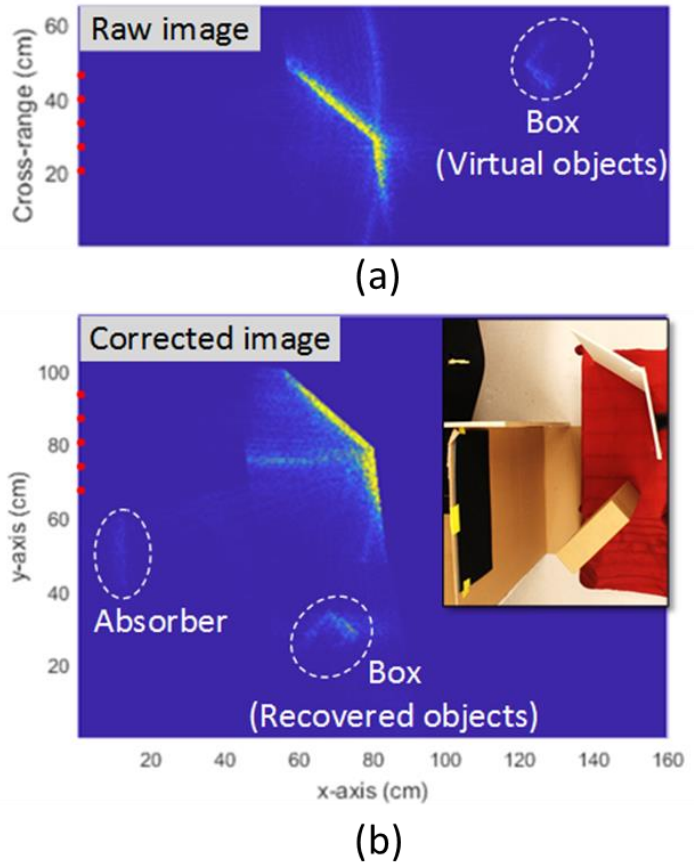

Figure 2.10- a) Raw SAR image obtained, the bright yellow line is the drywall, and the cardboard box shown in the wrong position and treated as "ghost". B) Corrected image with the right location of the box after applying the algorithm. Inset: optical image of the scene [31].

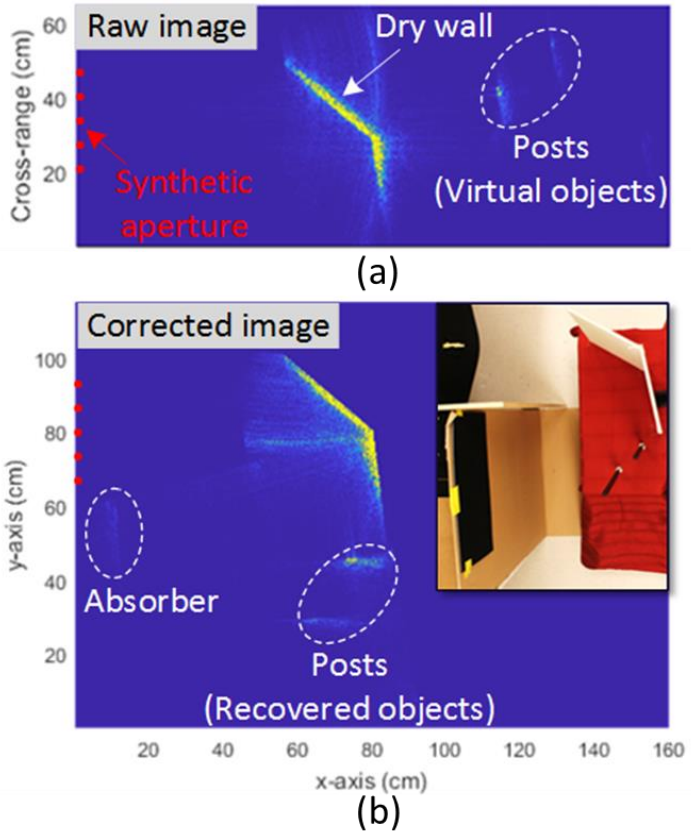

Figure 2.11- a) Raw SAR image obtained, the bright yellow line are the dry wall and the two dots are the "ghosts" that represents the metallic posts. b) Corrected image with the right location of the two posts after applying the algorithm. Inset: optical image of the scene [31].

CHAPTER 3

COMBINATION OF IMAGING AND AOA/RANGE ESTIMATION FOR SIMULTANEOUS LOCALIZATION AND MAPPING

In this chapter, the estimation of AoA and ToA or equivalently the range (range = ToA . speed of light) will be presented. We will discuss the signal model to find AoA in both cases: near field, and far field. Then the impact of these cases in our estimation on AoA will be analyzed. Finally, techniques used in ToA estimation in communications will be briefly introduced.

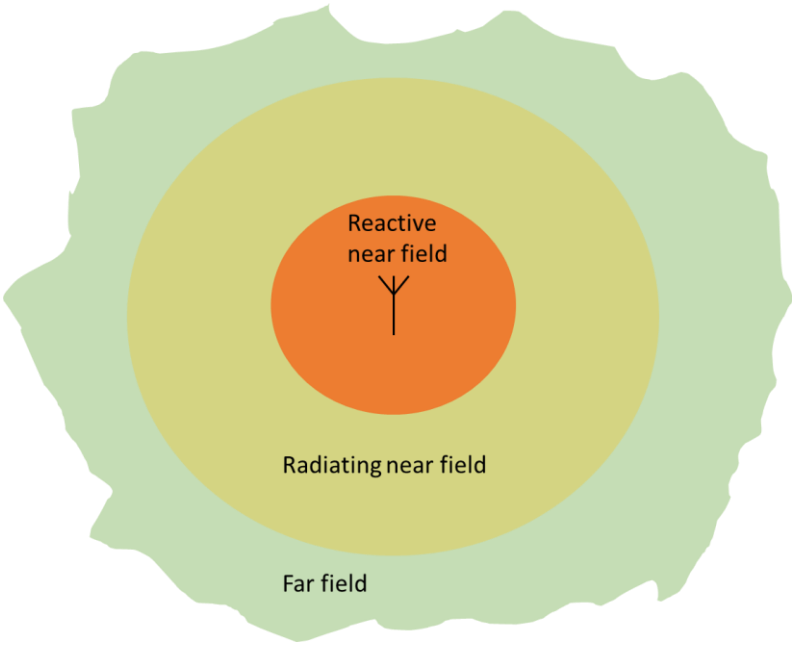

Figure 3.1- The three regions of EM fields of a radiating antenna.

3.1 Electromagnetic (EM) Fields Regions

The EM fields from a radiating element can be divided with respect of the area surrounding this element into 3 regions: reactive near field, radiating near field, and far field as shown in figure 3.1. These regions are separated by boundaries that when crossed define the fields pattern shape and characteristics and their details as follows:

a) Reactive near field

This region is defined as the immediate area around the radiating element, where the electric field component is in time-phase quadrature with magnetic field i.e. E-field and H-field are out of phase by 90° . All the power is stored therefore, the time average power density is equal to zero. The outer boundary of this region is given by [25]

$$R < 0.62\sqrt{\frac{D^3}{\lambda}} \qquad (3-1)$$

where *R* is the distance, *D* is the largest dimension of the radiating element "$D > \lambda$", if the largest dimension is smaller than λ then the boundary is taken as $\frac{\lambda}{2\pi}$.

b) Radiating near field

In this region the radiated power starts to dominate over the stored power, the angular fields components are dependent on the distance from the radiating elements and starts to from a spherical wave front. The boundaries of this region are given as [25]

$$0.62\sqrt{\frac{D^3}{\lambda}} < R < \frac{2D^2}{\lambda} \qquad (3-2)$$

If the radiating element largest dimension "D" is smaller than the wavelength then this region might not exist [25].

c) Far field

In this region, the fields components now are independent of the radial distance from the radiating element, and in this region, the fields can be treated as a plane wave. the inner boundary of this region is given by

$$R < \frac{2D^2}{\lambda} \qquad (3-3)$$

3.2 Received Signal Model for a Uniform Linear Array Receiver

In this section, we will consider finding the AoA from a phased antenna array system.

3.2.1 Near field Signal Model

Consider a signal $u(t)$ that is transmitted from a source that is at a radial distance R and angle θ in the near field from the center of the N element receiving array with reference element to respective n element spacing of d_n . Angle θ, ranges from 0 to π as shown in figure 3.2. Also, in this analysis, for simplicity but without loss of generality we assume $u(t)$ = 1. Since the source is in the near field region of the receiving array, no assumption is taken with regards to the radial distance from the target to each element of the array nor the angle θ. Hence, the need to select a reference distance/angle to determine the AoA from is needed. Any element can be chosen but for the sake of our analysis and later use in the algorithm the center element is chosen to be the reference.

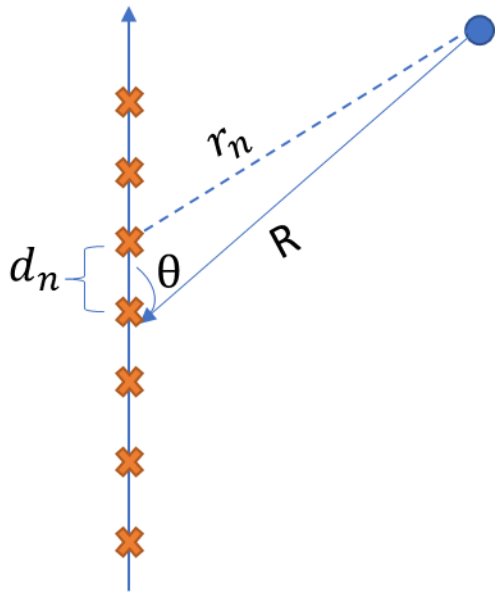

Figure 3.2- Near field representation of source at distance R from the center of the array, r_n is the distance from the nth element d_n is the spacing between each successive element , θ is the angle of of the source "AoA" measured from the axis of the array

For the center element, the phase variation incurred due to the source at a radial distance *R* is given by

$$e^{jkR} \qquad (3-4)$$

Similarly, the phase variation due to the same source at a radial distance r_n for an *n* element is

$$e^{jkr_n} \qquad (3-5)$$

In both equations, *k* is the wave number. Then, the phase different between the reference element and the *nth* element is:

$$e^{jk(r_n-R)} \qquad (3-6)$$

To estimate AoA, it is needed to relate equation (3-6) with the angle θ.

By looking into figure 3.2 and applying geometrical relations on the triangle depicted in that figure, r_n can be represent as [32]

$$r_n = \sqrt{(R\ sin\theta)^2 + (d_n - R\ cos\theta)^2} \qquad (3-7)$$

By expanding the brackets under the square root, equation (3-7) becomes

$$r_n = \sqrt{R^2 + 2d_n\ R\ cos\theta + d_n^2} \qquad (3-8)$$

Hence the array factor for an N element array can be expressed as [32]:

$$AF(\theta, R) = \sum_{n=0}^{N-1} a(m) * e^{jk\left(\sqrt{R^2+2d_m R\ cos\theta + d_m^2} - R\right)}; m = n - \frac{N-1}{2} \qquad (3-9)$$

Or in vector form, the array response vector is

$$g(\theta, R) = \begin{bmatrix} a\left(-\frac{N-1}{2}\right) e^{jk\left(r_{-\frac{N-1}{2}} - R\right)} \\ a\left(1 - \frac{N-1}{2}\right) e^{jk\left(r_{1-\frac{N-1}{2}} - R\right)} \\ \vdots \\ 1 \\ \vdots \\ a\left(N-2-\frac{N-1}{2}\right) e^{jk\left(r_{N-2-\frac{N-1}{2}} - R\right)} \\ a\left(N-1-\frac{N-1}{2}\right) e^{jk\left(r_{N-1-\frac{N-2}{2}} - R\right)} \end{bmatrix} \qquad (3-10)$$

In both (3-9) and (3-10) $a(m)$ represent the ratio of the attenuation of spherical waves and is given by $a(m) = \frac{R}{r_m}$ [33]. From (3-9) and (3-10), it is noticed that this a joint

search problem for both θ, and R in which both parameters can be estimated in the same search operation. For the sake of simplicity and throughout this thesis the reference distance R is assumed known or estimated via other range finding techniques as it will simplify the search and will give a greater focus on finding the AoA θ. Hence, the steering vector needed to be applied to match filter the array response vector $g(\theta, R)$ at θ=θ_{AoA} is $g^*(\theta = \theta_{AoA}, R)$ where * is the conjugate operator.

Note about even and odd numbered arrays:

For an odd array the element that can be chosen as a reference is the center element and all of the previous analysis above can be applied, however for an even-numbered array there is no center element hence either selecting one of the two center elements or create a virtual point in the center and apply the same analysis to it.

3.2.2 Far Field Signal Model

Similar to the near field model, consider a signal $u(t) = 1$ that is transmitted from a source that is at a radial distance R in the far field (i.e. R is assumed now to be very large), and angle θ from the receiving array with equal element spacing of d as shown in figure 3.4. Since the source now is in the far field region of the receiving array, assume that the wave originating from the source is planar. As such, AoA is the same for all the elements and the radial distance R is the approximately the same for all i.e. $r_1 = r_2 = r_3 = r_4 \approx R$ for figure 3.4. And as for the phase variation of an incident wave on the received elements, each successive element has an incurred phase incremented by

$d\cos(\theta)$ with respect of the previous element in the array. Thus, the array factor of the receiver array of N elements due to a source in the far field is [25]:

$$AF = \sum_{n=0}^{N-1} e^{jk\,nd\,cos(\theta)} \qquad (3-18)$$

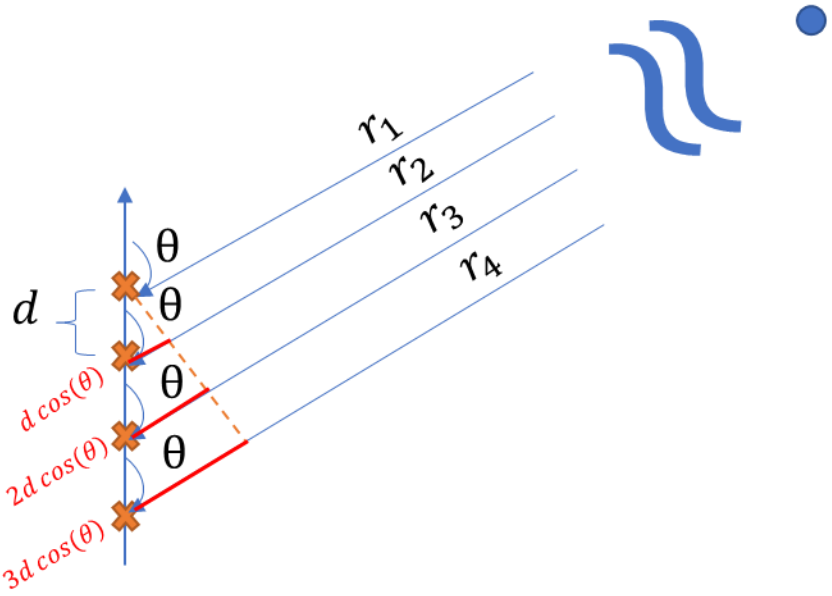

Figure 3.3- Far Field representation of a source that is transmitting to an receiving array . The travel paths from the source to each receiver point are assumed to be parallel with each other, and the signal is incident on them by the same angle θ. The red lines represent the extra phase incurred by each path compared to the first element path.

Or in vector form as array response vector

$$g(\theta) = \begin{bmatrix} 1 \\ e^{jkd\,cos(\theta)} \\ e^{jk2d\,\cos(\theta)} \\ \vdots \\ e^{jk(N-1)d\,\cos(\theta)} \end{bmatrix} \qquad (3-19)$$

As a consequence of the far field approximation, the angle information now is decoupled from the radial distance, and it is seen in equations (3-18), (3-19) that both the array factor and the steering vector are a function of θ only which simplify the angle search problem. The trade-off is the need to estimate the radial distance of the source via another approach if the scope of the problem is to estimate both angle and distance in which this work needs. Hence, the steering vector to be applied to match filter the array response vector $g(\theta)$ at $\theta=\theta_{AoA}$ is $g^*(\theta = \theta_{AoA})$, where $*$ is the conjugate operator .

3.3 Combining MmWave Imaging and AoA/ToA Information for SLAM

In this section, the algorithm to localize a mobile user by exploiting both mmWave imaging and AoA/ToA information is presented. First, as an initialize step, it is assumed the scene of interest is void from mobile stations i.e. only static objects are present. Then, the base station reconstructs a mmWave image and if necessary, correct it as explained in section 2.3. When a mobile user enters the environment, it will send a wideband uplink pilot signal that will be used to estimate AoA/ToA or equivalently AoA/range, as range R is equal to ToA*c_0. From the reconstructed image and the estimated AoA/Range information, there is three possible scenarios, the first one is that the mobile station is in direct line-of-sight with respect of the base station. The second is the mobile station is in the non-line-of-sight with respect of the base station, as depicted in figure 3.8, and finally, the mobile station is observed from both LoS and NLoS with respect of the base station.

The mmWave image will be combined with the estimated θ_{AoA} and ToA (range) to find the location of the user with respect to the environment. The physical center of the BS antenna array is used as a reference point for the θ_{AoA} and ToA. Namely, a ray is

launched from the BS center at an angle equal to θ_{AoA}. For LoS users, the length of the ray will be equal to *R*, and the user will be located at the end of the ray path. If the user is in NLoS, then the ray will intersect a mirror object at a distance <*R*. Then, a second ray is launched from the intersected point at the specular angle with respect to the mirror surface. This is repeated for multiple bounces until the total length of all the rays is equal to *R*. The end of the ray path is then the location of the user, as illustrated in figure 3.5 [34]. A flowchart summarizing this SLAM approach is laid out in figure 3.10.

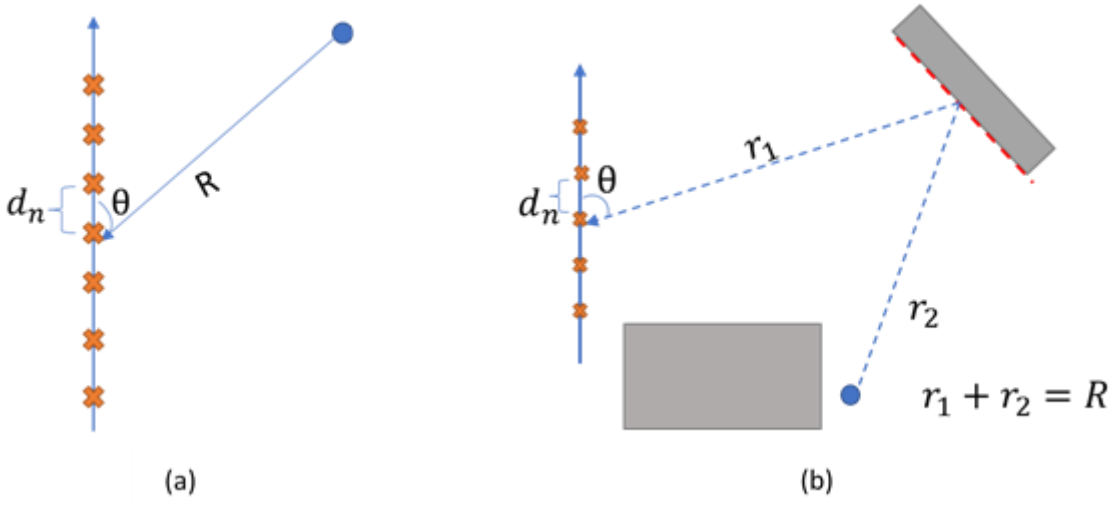

Figure 3.4- Example of user localization using a single base station equipped with an antenna array. (a) Mobile station is in LoS , (b) Mobile station is in NLoS.

In this chapter, the received signal model for both near and far fields were discussed to be used for AoA estimation highlight the difference in assumptions between them. Then, this thesis approach for high accuracy SLAM was presented and laid out with focusing on NLoS only localization by utilizing both mmWaves imaging and the AoA/ToA information together.

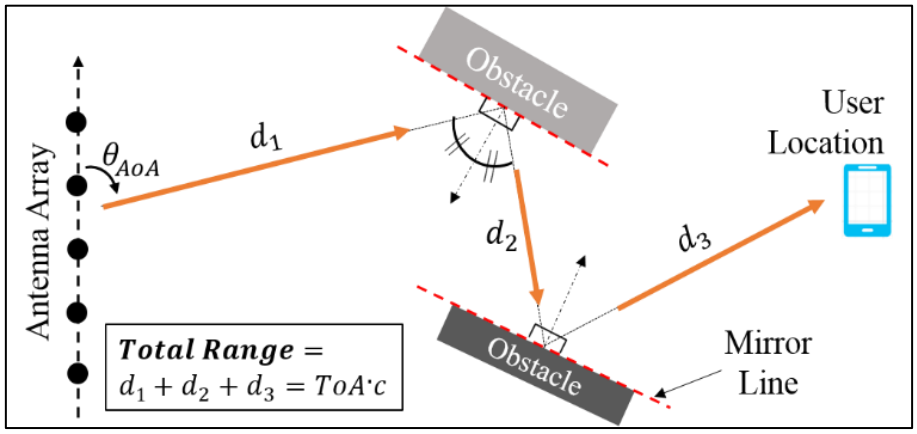

Figure 3.5- Projecting AoA/Range on the mmWave image and to recover the user location even for NLoS occasions [33] .

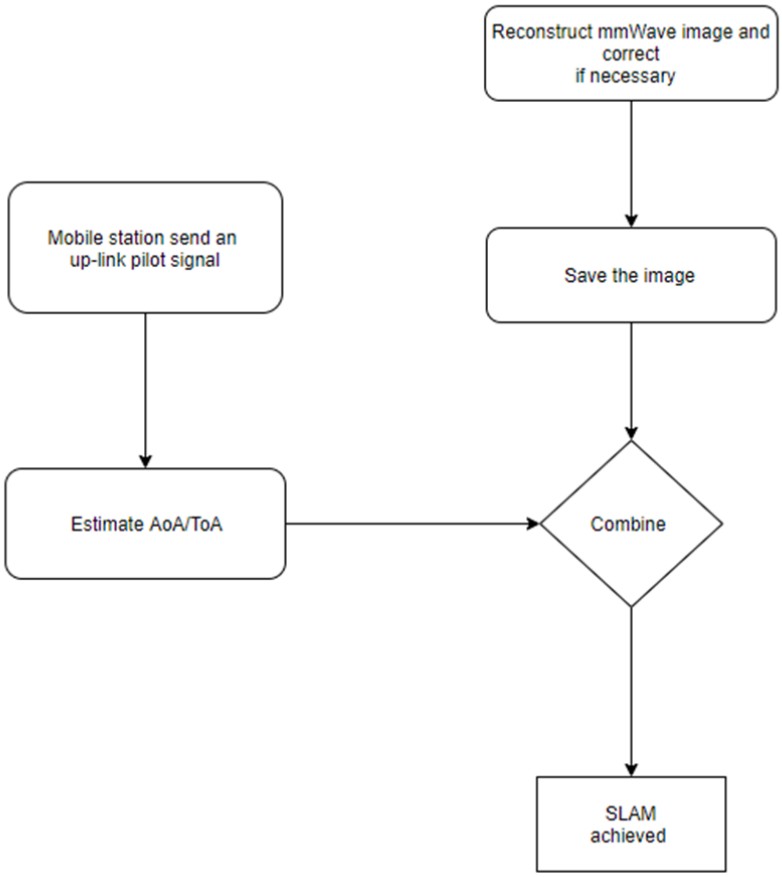

Figure 3.6- flowchart highlighting this SLAM approach process.

CHAPTER 4

SIMULATIONS AND MEASURMENTS RESULTS

In this chapter, the capability of the near field model to acquire the AoA information for both regions near/far field will be presented via simulations in various scenarios. Then, the SLAM algorithm will be verified both in simulations and lab measurements to demonstrate the effectiveness in localizing a user with centimeter accuracy.

4.1 Simulations

To analyze the novel SLAM method, we use full-wave simulation to estimate radiation, propagation, scattering and reception phenomena that occur in this complicated process. The simulated received signals are fed into the image reconstruction method (see Chapter 2, section 2.2) and AoA/range estimation (see Chapter 3, section 3.2) to estimate the methods performance. However, such geometries constitute extremely electrically large problems and full-wave EM solution becomes impractical. As such, we limit the analysis to 2D by using a commercial method-of-moments (MoM) solver (WiPL-D,[35]).

4.1.1 Near Field User Simulation Model

First, define a generating source that produces a 2D Gaussian beam that emulates a narrow beam and expressed as

$$Beam(x) = \frac{1}{\sigma\sqrt{2\pi}} e^{-\frac{x-\mu}{2\sigma^2}} \qquad (4-1)$$

Where μ, σ are the mean and standard deviation respectively and they are chosen to be as $\mu = 0, and\ \sigma = 0.1$. The far field pattern is shown in figure 4.1

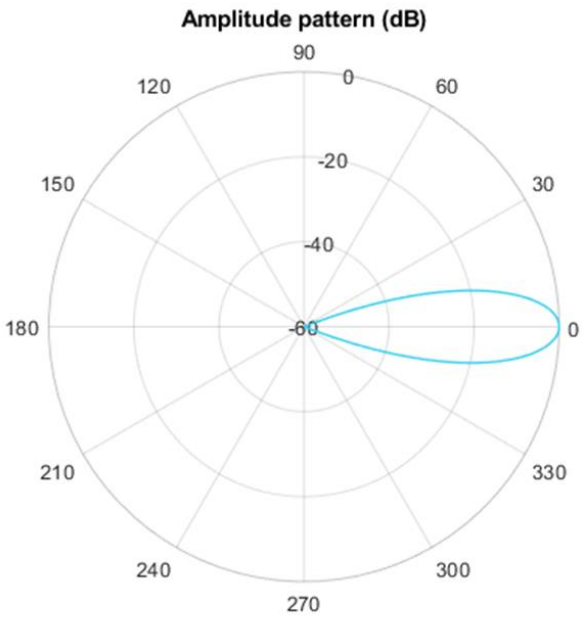

Figure 4.1- Polar plot of the far field pattern in dB for the 2D Gaussian narrow beam.

This source is operating at a frequency of 220 GHz which represents the user. It is placed at distance *R*= 1.8m from the center of 260 elements receiving array with equal spacing of 0.5 mm $\equiv \frac{\lambda}{3}$ at 220GHz in two direction: Broadside and a shifted 20 degree with respect of broadside as shown in figure 4.2. For the sake of this simulation and simplicity, the distance *R*=1.8m is assumed to be known or estimated from ToA methods.

First, fields data are collected for each element in the array which will represent the array response vector as defined in equation 3-10. Then, the steering vectors will be calculated using the conjugate of this equation covering all the possible angles from 0 to 180 degree

with an angle step of $\frac{180}{1000}$. These steering vectors will be multiplied with the response vector to recreate the received signal pattern.

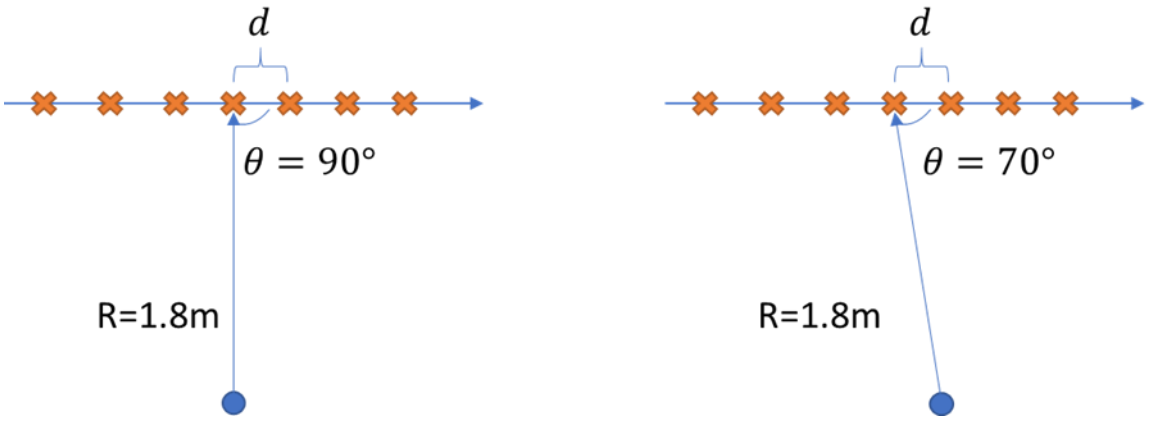

Figure 4.2- Near field simulation setup for a user at distance of 1.8 m from the center the receiver array. (a) the user is at broadside. (b) the user is shifted 20 degree "70 degree" from the broadside direction.

These steering vectors will be multiplied with the response vector to recreate the received signal pattern. This process is also known as digital beam forming (DBF) where the received fields are scanned for all possible angles and reconstruct the received pattern in post-processing. As shown in figure 4.3 and 4.4, both amplitude patterns have only single major lobe at their estimated direction. This is expected since the spacing between the elements is $\lambda/3 < \lambda/2$, and any spacing that is less than or equal to $\lambda/2$ for uniform linear scanning array will yield only a single peak [25].

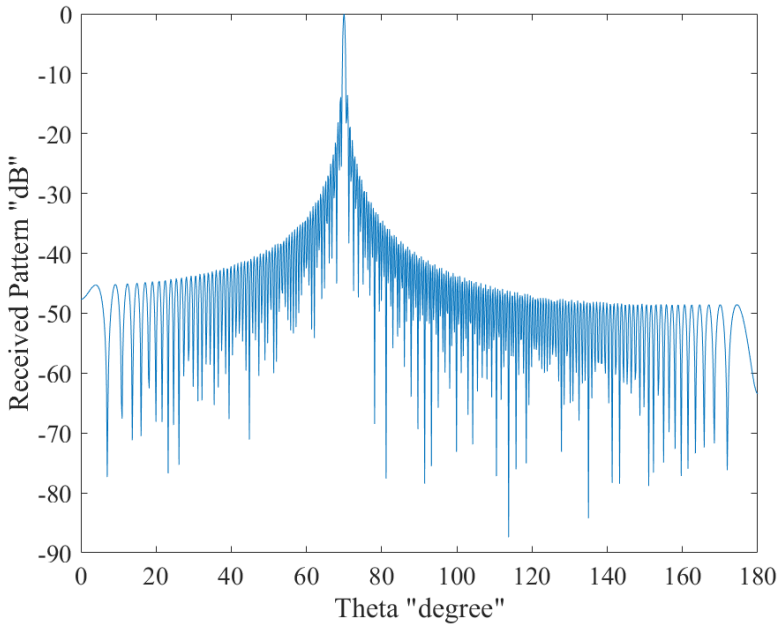

Figure 4.3- Received array response for a 20 degree shift with respect of broadside user in the near field at 220 GHz and distance of 1.8m. The maximum is at 70 degree which represents the real direction of the user.

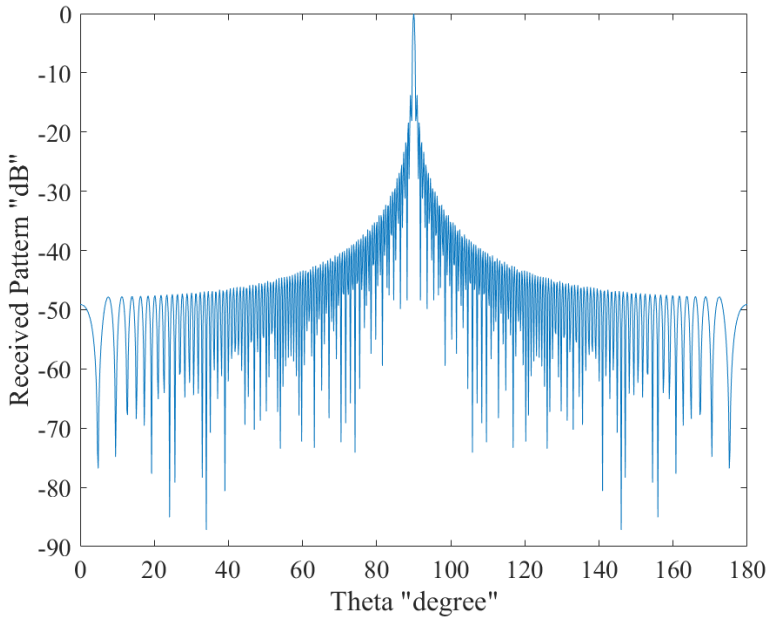

Figure 4.4- Received array response for a broadside user in the near field at 220 GHz and distance of 1.8m. The maximum is at 90 degree which represents the real direction of the user

4.1.2 Far-field User Simulation Model

The same generator source defined at section 4.1.1 is now placed at distance *R*= 20m to the center of 260 elements receiving array with equal spacing of 0.5 mm ≡λ/3 at 220GHz. This twenty-meter distance is chosen such that to make sure that the user now is in the far field region with respect to the receiving array. Two directions were considered broadside and a shifted 20 degree with respect of broadside as shown in figure 4.5.

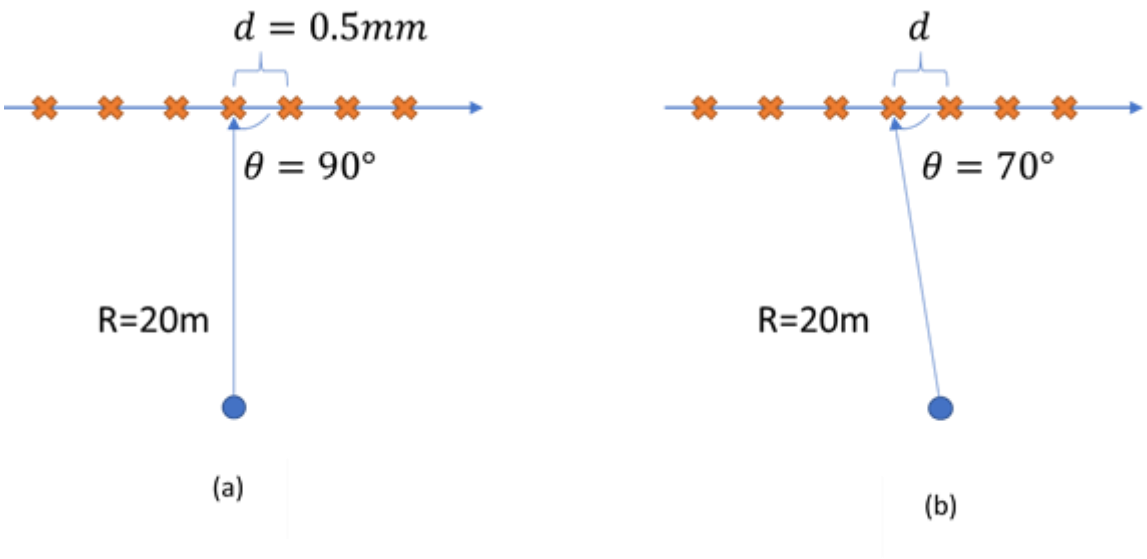

Figure 4.5- Far field simulation setup for a user at distance of 20 m from the center the receiver array. (a) the user is at broadside. (b) the user is shifted 20 degree "70 degree" from the broadside direction.

The near field model of section 3.2.1 is used to demonstrate the capability of the defined array response vector to model both regions near/far field, as this model is general and doesn't make any assumption regarding what region it is. Similar to the previous section, the steering vectors will be calculated using the conjugate of equation 3-10 for all possible angles. Then, they will be multiplied with the response vector to recreate the received signal pattern in the far field, and for comparison, the pattern is also calculated using the far field approximation as outlined in chapter 3. The results are shown in figure 4.6 and 4.7. From both figures 4.6 and 4.7, it can be noticed that both the

near field model and the far field model are in agreement with each other. This is expected as the near field model can account for all possible distances.

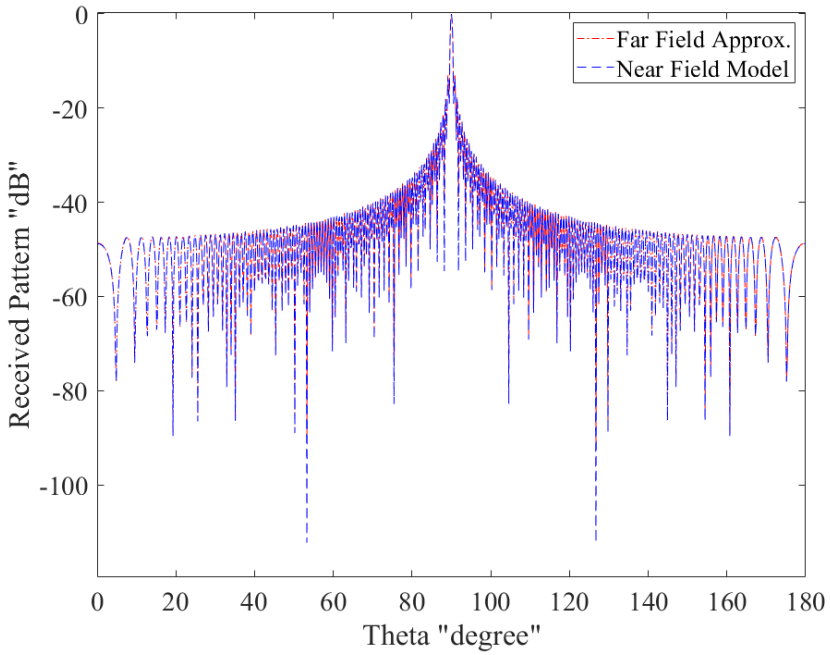

Figure 4.6-Received array response for a broadside user in the far field at 220 GHz and distance of 20 m. The red line represents the recreated pattern using the far field approximation, while the blue line is recreated using the near field model, as seen for both cases, the maximum is at 90 degree which represents the real direction of the user.

4.1.3 SLAM Simulation for a 2D Scene

Consider the following 2D scenario, a user represented by a gaussian narrow beam of equation 4-1 and is operating at a bandwidth of 75 GHz with a frequency range from 220 GHz to 295 GHz. This user is placed at a distance 1m from the center of 40 cm rough PEC wall with an angle of 45 degrees with respect to the wall normal. Then, 260 elements with equal spacing of 0.5 mm that will create a monostatic SAR are placed at 0.8 m from the center of the rough PEC wall as illustrated in figure 4.8.

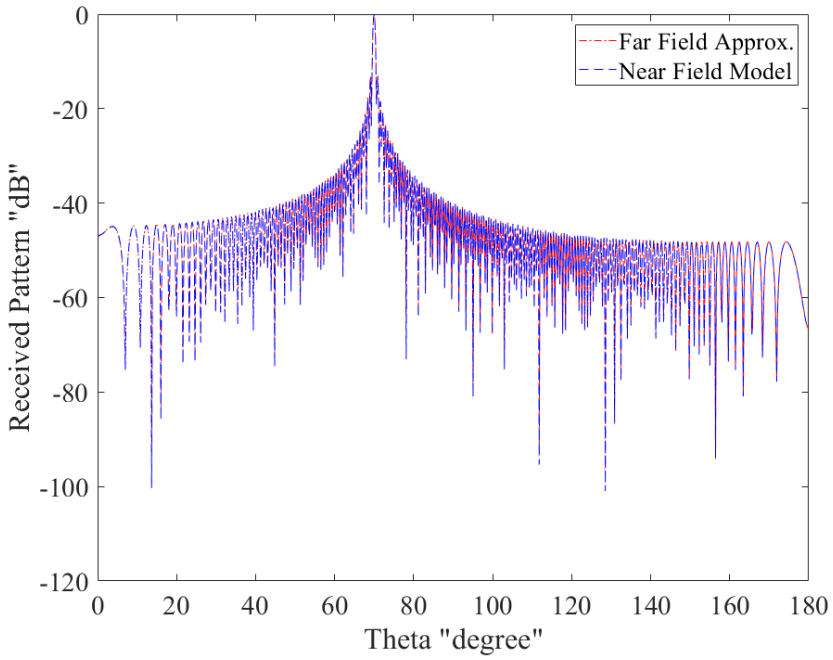

Figure 4.7- Received array response for a 20 degree shift with respect of broadside user in the far field at 220 GHz and distance of 20 m. The red line represents the recreated pattern using the far field approximation, while the blue line is recreated using the near field model, as seen for both cases, the maximum is at 70 degree which represents the real direction of the user.

First, the monostatic SAR is used to illuminate and records the fields for 1001 frequency points for the defined bandwidth which yields a maximum allowable range of 1 m and range resolution of 2 mm. This recorded data then is used to reconstruct the 2D mmWave image as shown in figure 4.9. Since there is only a single static object in this simple scenario there is no merit in applying image correction and this single object is defined as the reflective surface. Then, the user transmits tones using stepped frequency in the same defined frequency range that emulates ToA and is captured by the SAR in which they will be used to create the AoA/range map as shown in figure 4.10 for a single frequency AoA and figure 4.11 for the AoA/range map.

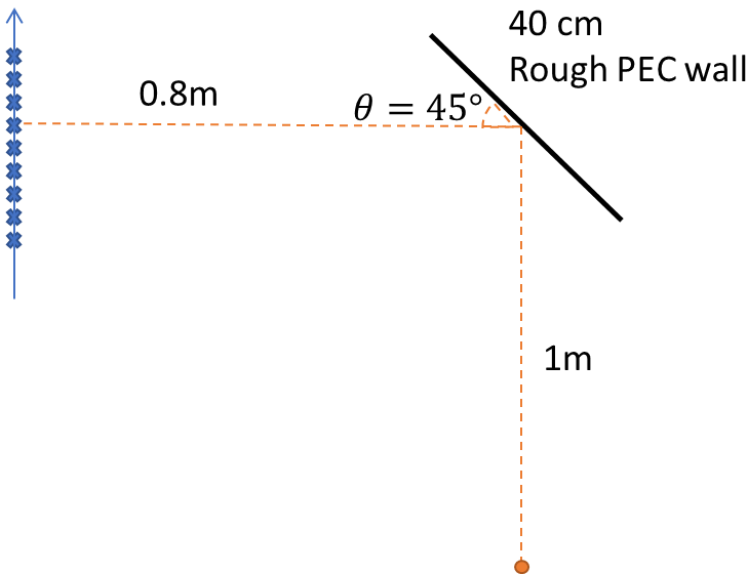

Figure 4.8- User is placed 1 m away from a rough PEC wall with an angle of 45 degree with respect of the normal of the wall. A receiver array is placed 0.8 m away from center of the wall

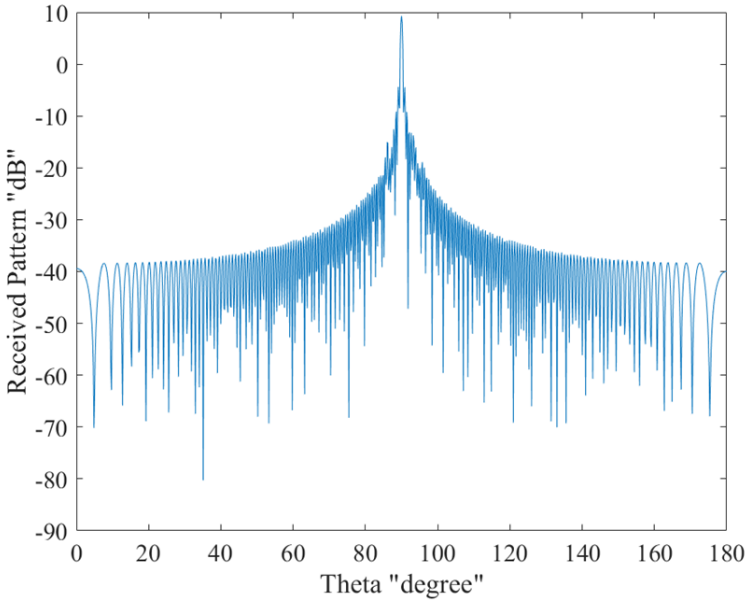

Figure 4.9- AoA estimation of a single frequency at 220 GHz, the user appears wrongfully to be in the broadside with respect to the SAR.

Finally, the AoA/Range map information is projected upon the mmWave image as outlined in section 3.5 to achieve SLAM, and the results are shown in figure 4.12. The results of SLAM are in strong agreement with simulation parameters with a deviation of less than 1 mm, and the cross range resolution is about 11 mm for a distance of 1.8m.

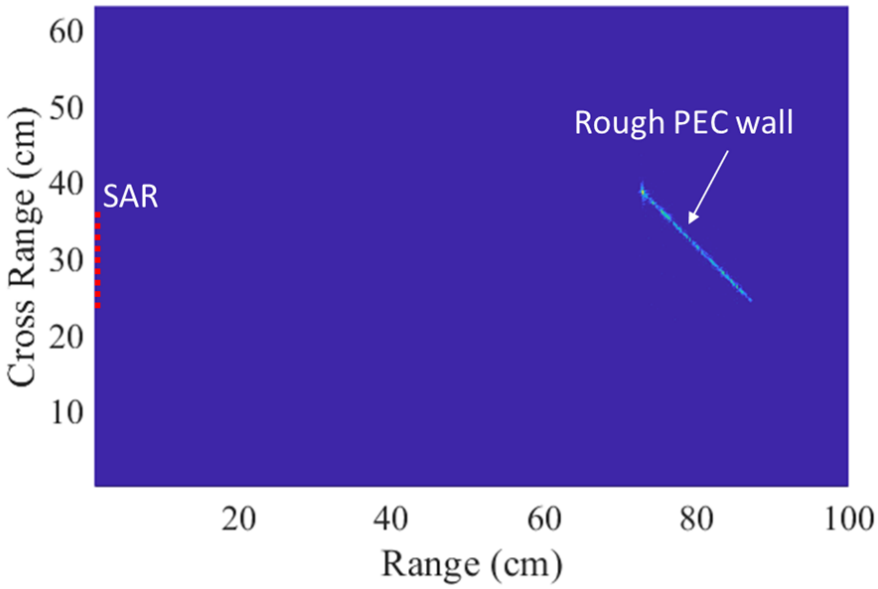

Figure 4.10- Reconstrued mmWave image highlighting the rough wall and SAR. This image has range resolution of 2mm.

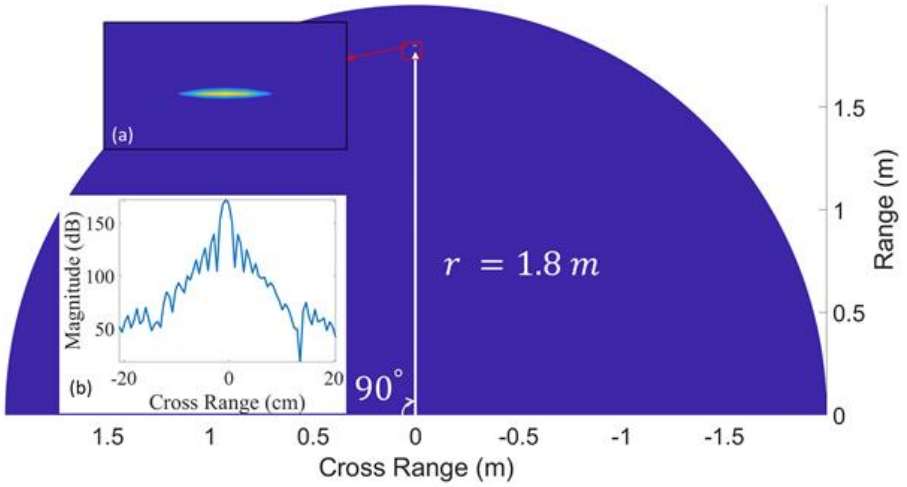

Figure 4.11- AoA/Range map from the estimated information of AoA/ToA of the recorded data. The user appears wrongfully to in the broadside at distance of 1.8 m with respect to the imaging aperture. Inset: a) a highlighted portion of the map showing the top view at 1.8 m. b) Cross-section of user amplitude peak.

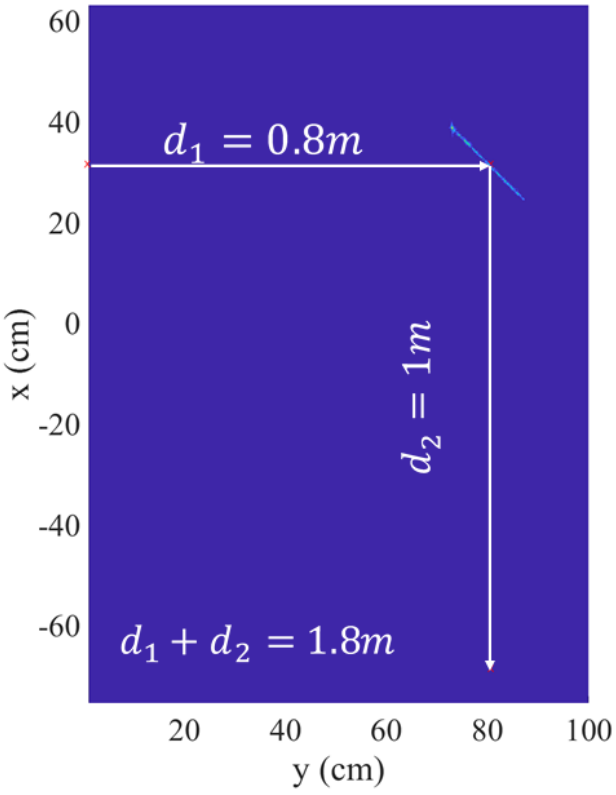

Figure 4.12- The localization of the user after projection for the simulated 2D scene.

4.2 Measurements

An experiment for SLAM carried in THz lab is performed by setting up a 2D environment that consists of two VNA extenders [36] connected to two 23 dBi horn antenna are mounted on a one-dimensional motorized linear stage that will create a 13 cm monostatic synthetic aperture in which represent the base station. While for the user, it is represented by a single VNA extender connected to 23 dBi horn antenna as well. Finally, two drywalls one is in LoS while the other in NLoS of the base station are placed as shown in figure 4.13.

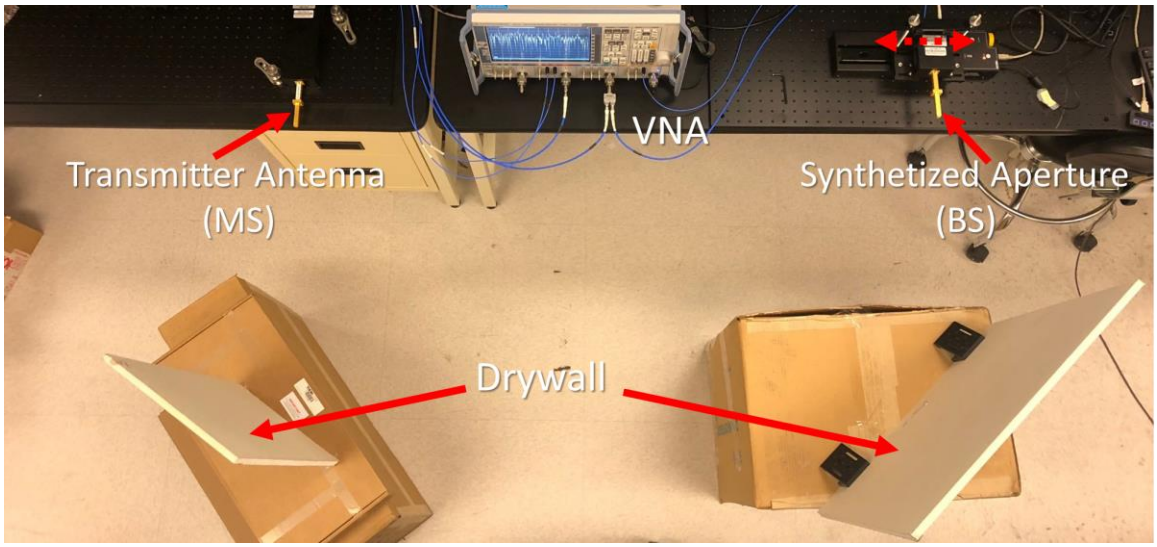

Figure 4.13-2D experiment setup, as shown two drywalls are placed in line of sight and non-line of sight of motorized VNA extender that will act as a base station. While another VNA extender will act as a user that is going to be localized [32].

The frequencies range of operation is from 220-330 GHz that gives a100 GHz bandwidth which yields a range resolution of 1.5 mm. For both the base station "imaging system" and the user a stepped-frequency signal is transmitted along this bandwidth with frequency step size of 20 MHz for a total of 5500 points. This enables the maximum allowable rage of approximately 3.75 m for the imaging system. The synthesized aperture illuminates the scene and record S_{21} for the multiple frequency points in the defined

frequency range. This recorded data will be used to reconstruct the raw mmWave image and then correct it using the approach outlined in chapter 2, the results are shown in figure 4.14 and 4.15.

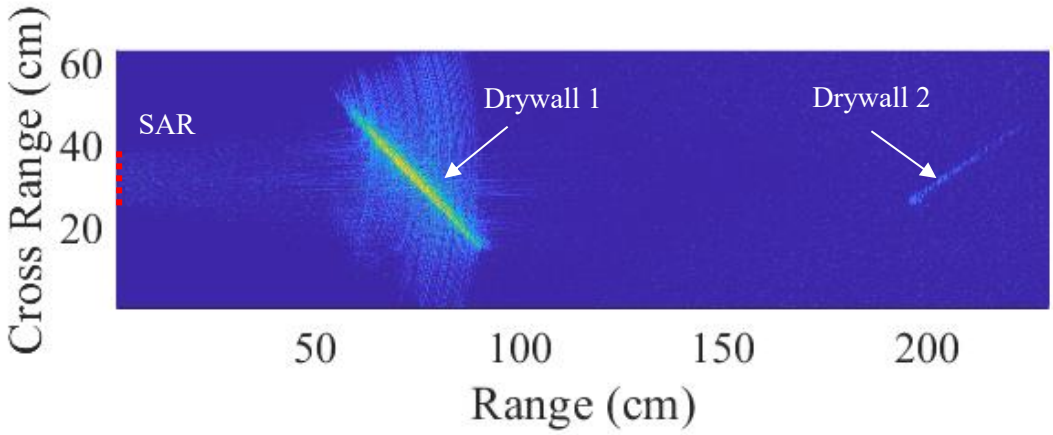

Figure 4.14- Reconstrued raw mmWave image of the 2D environment. The 2nd NLoS drywall appears behind the LoS drywall erroneously and needs correction [34].

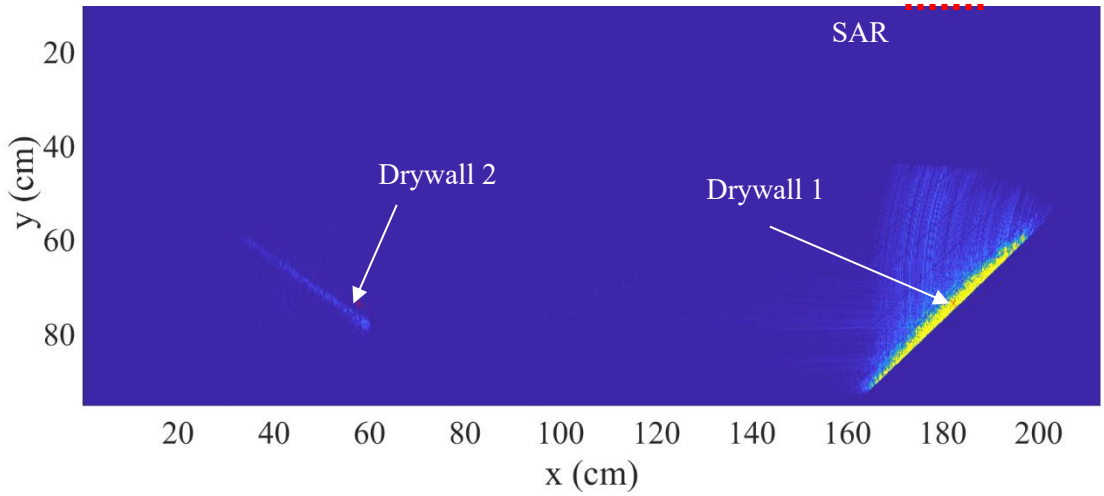

Figure 4.15- Corrected mmWave image. Now, the 2nd dry wall is placed at the correct position [34].

Then, the user sends tones in the same frequency range using stepped frequency that emulate ToA that is captured by the base station and are recorded as S_{21}as well. By applying the AoA/ToA (range) estimation techniques to the recorded data, an AoA/range map is obtained as shown in figure 4.16. Finally, this AoA/Range information is projected on the corrected image with the outlined algorithm described in section 3.5 to achieve SLAM for the user as seen in figure 4.17. The results are verified with the actual distances using measuring tools and are in good agreement with the experiment results within centimeter accuracy ≈ 3mm. As for the cross-range resolution, it is approximately 2.6 cm at distance of 2.8m for the 13cm synthesized aperture.

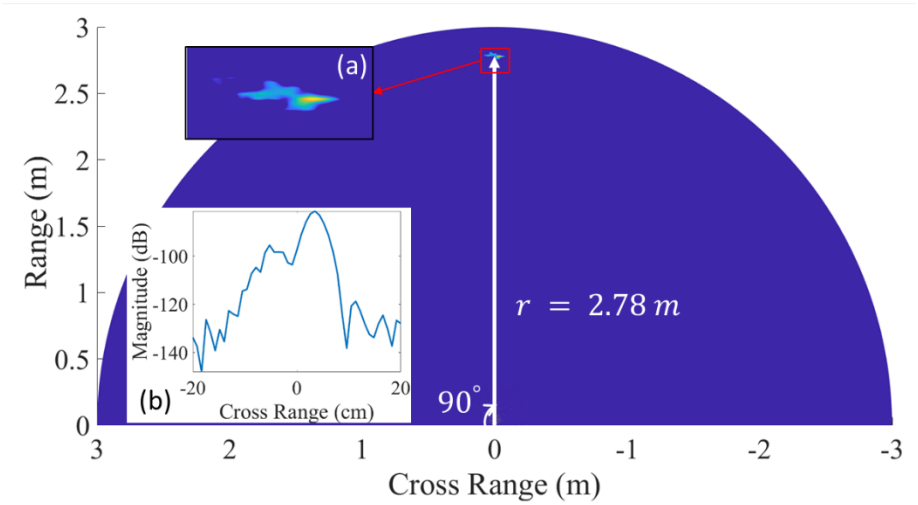

Figure 4.16- AoA/Range map from the estimated information of AoA/ToA of the recorded data. The user appears wrongfully to in the broadside at distance of 2.78m with respect to the imaging aperture. Inset: a) a highlighted portion of the map showing the top view at 2.78 m. b) Cross-section of user amplitude peak.

In this chapter, both simulations and measurements were carried out to verify this thesis approach for SLAM. First, AoA simulations both in the near/far field were carried out and showed accurate angle localization for both cases and demonstrated the ability of the near field model to localize the angle even in far field scenarios. Then, a simple 2D SLAM scenario was simulated and was able to correctly localize the user with 2 mm range resolution and resolvable length of 11 mm at distance of 1.8. Finally, measurements were carried out in the lab to simulate 2 bounces NLoS SLAM scenario in which the proposed approach is able to correctly identify the user with centimeter accuracy as mentioned in this chapter.

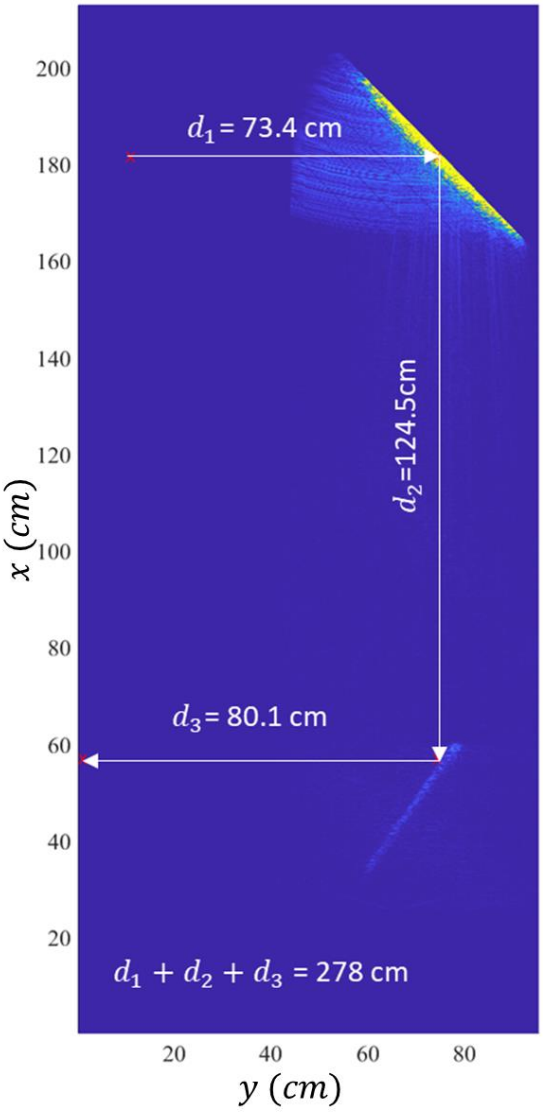

Figure 4.17- the localization of the user after projection into the corrected 2D image [34].

CHAPTER 5

CONCLUSIONS AND FUTURE WORK

5.1 Conclusions

In this thesis, centimeter accuracy SLAM is achieved by combining mmWave imaging and AoA/ToA estimation. The main goal of this work is to demonstrate the ability to localize users in the non-line-of-sight only with multiple reflections scenario with high accuracy. It is done that by exploiting both specular and diffuse scattering of mmWave signal due to surface roughness. As such, mmWaves are utilized to image both LoS and NLoS objects with millimeter-scale range. Then, AoA models for both near/far field regions are used to obtain the direction of signal arrival are presented.

To validate the accuracy of this approach, 2D full-wave simulations were carried out to estimate the AoA for several scenes. First, for LoS only in the frequency of 220 GHz scenario, it was demonstrated that the near field model can accurately estimate AoA and it is was identical to the far field approximation model when compared in the far field region. Moreover, a simple SLAM scenario is simulated where a mmWave image is reconstructed using a 13 cm monostatic SAR. This SAR operates in the range of 220-295 GHz which yields a total bandwidth of 75 GHz with range resolution of 2 mm. Also, a source that emulates a user is placed in the NLoS with respect to the receiver transmits discreet frequency pilot signals within the 220-295 GHz bandwidth. By applying the Fourier Transform on the discreet frequency tones, we estimate both AoA and range which are then projected on the mmWave image. This will finally lead to the true localization of the user achieving centimeter accuracy in range and cross-range resolution of 11 mm at a distance of 1.8m

Furthermore, experimental measurements were carried out in the lab for a 2D non-LoS scenario with multiple reflections that used 23 dBi Horn antenna coupled to VNA extenders to emulate both the base station and the user in the frequency range of 220-330 GHz. Both mmWave image and AoA/ToA information are acquired, then the AoA/ToA information is projected onto the mmWave. The user was localized correctly demonstrating the capability of this approach to localize NLoS users from multiple reflections with a centimeter (3mm) accuracy in range and cross-range resolution of approximately 2.6 cm at distance of 2.8m for the 13cm synthesized aperture.

5.2 Future work

However, there are many challenges and improvements that can be addressed in subsequent studies. The following points summarize such challenges:

- Investigate the localization of a user where diffuse scattering signals dominate the multipath propagation. The loss of the specular direction information will result in localization ambiguity.
- The process of identifying the reflective surface boundary for image correction in this work is carried out manually. Future work will focus on the implementation of an algorithm that automates the process by identifying mirror surfaces and applying the mirroring correction.
- Although the focus of this work is for SLAM, this work can be extended and used in mmWave channel estimation in wireless communications, thus leading to the reduction of training overhead which will lead to increased data rates.

REFRENCES

[1] "'Christian Huelsmeyer, the inventor.'" [Online]. Available: http://www.radarworld.org/huelsmeyer.html. [Accessed: 12-May-2019].

[2] T. Bailey and H. F. Durrant-Whyte, "Simultaneous localization and mapping (SLAM): Part I," *IEEE Robot. Autom. Mag.*, vol. 13, no. 3, pp. 108–117, 2006.

[3] G. C. Trichopoulos, H. L. Mosbacker, D. Burdette, and K. Sertel, "A broadband focal plane array camera for real-time thz imaging applications," *IEEE Trans. Antennas Propag.*, vol. 61, no. 4, pp. 1733–1740, 2013.

[4] D. M. Sheen, D. L. McMakin, and T. E. Hall, "Three-dimensional millimeter-wave imaging for concealed weapon detection," *IEEE Trans. Microw. Theory Tech.*, vol. 49, no. 9, pp. 1581–1592, 2001.

[5] K. Witrisal *et al.*, "High - Accuracy Localization for Assisted Living," no. March, pp. 59–70, 2016.

[6] G. Reitmayr *et al.*, "Simultaneous localization and mapping for augmented reality," *Proc. - 2010 Int. Symp. Ubiquitous Virtual Reality, ISUVR 2010*, pp. 5–8, 2010.

[7] M. Csorba, S. Clark, P. Newman, H. F. Durrant-Whyte, and M. W. M. G. Dissanayake, "A solution to the simultaneous localization and map building (SLAM) problem," *IEEE Trans. Robot. Autom.*, vol. 17, no. 3, pp. 229–241, 2002.

[8] "THE FUTURE OF AR IS SLAM TECHNOLOGY. BUT WHAT IS SLAM?" [Online]. Available: https://www.analyticsinsight.net/future-ar-slam-technology-slam.

[9] "Amazon deploys fleet of robotic 'elves.'" [Online]. Available: www.marketwatch.com/story/amazon-deploys-fleet-of-robotic-elves-2014-12-01.

[10] "Global Positioning System." [Online]. Available: https://www.gps.gov/.

[11] F. Zafari, A. Gkelias, and K. Leung, "A Survey of Indoor Localization Systems and Technologies," pp. 1–32, 2017.

[12] S. Grant, "RHO-RHO LORAN-C COMBINED WITH SATELLITE NAVIGATION FOR OFFSHORE SURVEYS," *Int. Hydrogr. Rev.*, vol. XXIII, 1973.

[13] S. Challa, F. Leipold, S. K. Deshpande, and M. Liu, "Simultaneous Localization and Mapping in Wireless Sensor Networks," in *2005 International Conference on Intelligent Sensors, Sensor Networks and Information Processing*, 2005, pp. 81–87.

[14] Z. Wei, Y. Zhao, X. Liu, and Z. Feng, "DoA-LF: A Location Fingerprint Positioning Algorithm with Millimeter-Wave," *IEEE Access*, vol. 5, no. c, pp.

22678–22688, 2017.

[15] M. Kotaru, K. Joshi, D. Bharadia, and S. Katti, “Kotaru et al. - Unknown - SpotFi Decimeter Level Localization Using WiFi.pdf,” pp. 269–282.

[16] D. Vasisht, S. Kumar, and D. Katabi, “Decimeter-level Localization with a Single WiFi Access Point,” in *Proceedings of the 13th Usenix Conference on Networked Systems Design and Implementation*, 2016, pp. 165–178.

[17] N. Maletic, V. Sark, J. Gutierrez, and E. Grass, “Device Localization Using mmWave Ranging with Sub-6-Assisted Angle of Arrival Estimation,” *IEEE Int. Symp. Broadband Multimed. Syst. Broadcast. BMSB*, vol. 2018-June, pp. 4–9, 2018.

[18] J. Palacios, P. Casari, and J. Widmer, “JADE: Zero-knowledge device localization and environment mapping for millimeter wave systems,” *Proc. - IEEE INFOCOM*, 2017.

[19] A. Shahmansoori, G. E. Garcia, G. Destino, G. Seco-Granados, and H. Wymeersch, “Position and Orientation Estimation Through Millimeter-Wave MIMO in 5G Systems,” *IEEE Trans. Wirel. Commun.*, vol. 17, no. 3, pp. 1822–1835, 2018.

[20] K. B. Cooper, R. J. Dengler, N. Llombart, B. Thomas, G. Chattopadhyay, and P. H. Siegel, “THz imaging radar for standoff personnel screening,” *IEEE Trans. Terahertz Sci. Technol.*, vol. 1, no. 1, pp. 169–182, 2011.

[21] S. S. Ahmed, A. Schiessl, and L. P. Schmidt, “A novel fully electronic active real-time imager based on a planar multistatic sparse array,” *IEEE Trans. Microw. Theory Tech.*, vol. 59, no. 12 PART 2, pp. 3567–3576, 2011.

[22] X. Gu, A. Valdes-Garcia, A. Natarajan, B. Sadhu, D. Liu, and S. K. Reynolds, “W-band scalable phased arrays for imaging and communications,” *IEEE Commun. Mag.*, vol. 53, no. 4, pp. 196–204, 2015.

[23] “Cascaded Radar And Body&Chassis Automotive Applications.” [Online]. Available: https://training.ti.com/sites/default/files/docs/cascaded-radar-and-body_chassis-automotive-applications.pdf.

[24] M. Soumekh, *Synthetic Aperture Radar Signal Processing with MATLAB Algorithms*. New York: J. Wiley, 1999.

[25] C. A. Balanis, *Antenna Theory: Analysis and Design*, 4th ed. John Wiley and Sons, 2016.

[26] X. Li, B. Deng, Y. Qin, J. Gao, and H. Wang, “A Novel Method for 3-D Millimeter-Wave Holographic Reconstruction Based on Frequency Interferometry Techniques,” *IEEE Trans. Microw. Theory Tech.*, vol. 66, no. 3, pp. 1579–1596, 2018.

[27] G. Yates, A. M. Home, A. P. Blake, and R. Middleton, “Bistatic SAR image formation,” *IEE Proc. - Radar, Sonar Navig.*, vol. 153, no. 3, pp. 208–213, Jun.

2006.

[28] Ahmed S.S, *Electronic Microwave Imaging with Planar Multistatic Arrays*. Logos Verlag Berlin GmbH, 2014.

[29] M. C. Yoo, "(12) United States Patent VERTICAL TOPOLOGY LIGHT EMITTING (45) Date of Patent :," *Electron. Lett.*, vol. 2, no. 12, pp. 7–8, 2012.

[30] D. Novotny, R. A. Chamberlin, J. Gordon, N. Popovic, and E. N. Grossman, "Submillimeter Wavelength Scattering From Random Rough Surfaces," *IEEE Trans. Terahertz Sci. Technol.*, vol. 7, no. 5, pp. 546–562, 2017.

[31] S. K. Doddalla and G. C. Trichopoulos, "Non-Line of Sight Terahert Imaging from a Single Viewpoint," *IEEE MTT-S Int. Microw. Symp. Dig.*, vol. 2018-June, pp. 1527–1529, 2018.

[32] R. Kennedy and T. D. Abhayapala, "Broadband nearfield beamforming using a radial beampattern transformation," *Signal Processing*, vol. 46, no. 8, pp. 2147–2156, 2002.

[33] S. Doclo and M. Moonen, "Design of far-field and near-field broadband beamformers using eigenfilters," *Signal Processing*, vol. 83, no. 12, pp. 2641–2673, 2003.

[34] M. Aladsani, A. Alkhateeb, and G. C. Trichopoulos, "Leveraging mmWave Imaging and Communications for Simultaneous Localization and Mapping," pp. 4539–4543, 2018.

[35] "WiPL-D." [Online]. Available: https://wipl-d.com/.

[36] "Virginia Diodes, Inc," 2018. [Online]. Available: Vadiodes.com.